

# DynamicPAE: Generating Scene-Aware Physical Adversarial Examples in Real-Time

Jin Hu , Xianglong Liu , Member, IEEE, Jiakai Wang , Junkai Zhang , Xianqi Yang, Haotong Qin , Yuqing Ma , and Ke Xu

**Abstract**—Physical adversarial examples (PAEs) are regarded as “whistle-blowers” of real-world risks in deep-learning applications, thus worth further investigation. However, current PAE generation studies show limited adaptive attacking ability to diverse and varying scenes, revealing the emergency requirement of dynamic PAEs that are generated in real-time and conditioned on the observation from the attacker. The key challenges in generating dynamic PAEs are exploring their patterns under noisy gradient feedback and adapting the attack to agnostic scenario natures. To address the problems, we present DynamicPAE, the first generative framework that enables scene-aware real-time physical attacks beyond static attacks. Specifically, to train the dynamic PAE generator under noisy gradient feedback, we introduce the residual-driven sample trajectory guidance technique, which is mainly achieved by redefining the training task to break the limited feedback information restriction that leads to the degeneracy problem. Intuitively, it allows the gradient feedback to be passed to the generator through a low-noise auxiliary task, thereby guiding the optimization away from degenerate solutions and facilitating a more comprehensive and stable exploration of feasible PAEs. To adapt the generator to agnostic scenario natures, we introduce the context-aligned scene expectation simulation process, consisting of the conditional-uncertainty-aligned data module and the skewness-aligned objective re-weighting module. The former enhances robustness in the context of incomplete observation by employing a conditional probabilistic model for domain randomization, while the latter facilitates consistent stealth control across different attack targets by automatically reweighting losses based on the skewness indicator. Extensive digital and physical evaluations demonstrate the superior attack performance of DynamicPAE, attaining a  $1.95\times$  boost (65.55% average AP drop under attack) on representative object detectors (e.g., Yolo-v8) over state-of-the-art static PAE generating methods. Overall, our work opens the door to end-to-end modeling of dynamic PAEs by overcoming the uncertainty inherent in their generation.

**Index Terms**—Adversarial Example, Physical Adversarial Attack, Object Detection, Dynamic Physical Adversarial Example

## 1 INTRODUCTION

NUMEROUS intelligent applications in real-world scenarios have been landed in recent years, such as autonomous driving [1], healthcare [2] and intelligent assistant [3]. However, adversarial examples (AEs), which are specially designed for misleading machine learning models [4], have long been a challenge for deep learning applications [5]. Among them, the physical-world adversarial examples (PAEs) are attracting broader attention due to their feasibility in the real world and de facto threats to business AI systems [6]–[9]. Besides revealing the risks, the research on AEs (PAEs) also deepens the understanding of deep neural networks and reveals their defects in industrial and science applications [10], [11]. Therefore, modeling AEs, especially PAEs, is worth further investigating to alleviate the trustworthy issues (e.g., interpretability, security, and robustness) of deep learning models and related applications.

The existing adversarial attacks can be categorized as digital attacks and physical attacks, carried out in digital and real-world scenarios, respectively. On this basis, a line of studies aims to further propose adversarial attacks and

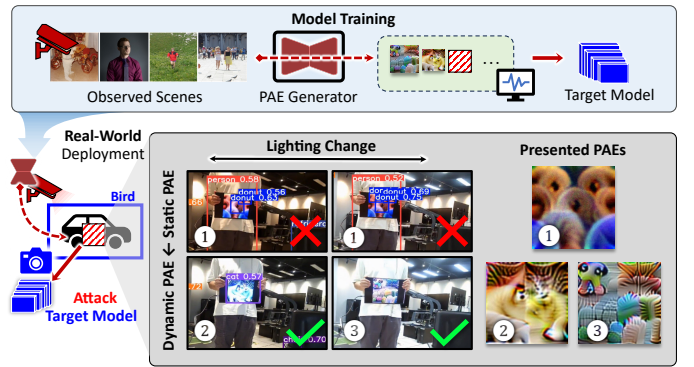


Figure 1: DynamicPAE framework trains real-time scene-aware physical adversarial example (PAE) generators and establishes the novel form of PAE, i.e., *dynamic PAE*.

promote the explainability of deep learning models [12]–[15]. Another line of research focuses on realizing PAEs in real-world settings [16], [17], as digital AEs may not be robust when fabricated in the real world [18]. In terms of threat, PAEs pose greater social risks, therefore highly attracting broader focuses. However, mainstream PAE methods address the real-world PAE generation problem by treating it as a static issue, either attempting to generalize the PAE across all simulated physical scenes [19] or requiring retraining each time to adapt to new settings [20]. This approach results in inadequate adaptability and generation

• Jin Hu, Xianglong Liu, Junkai Zhang, Yuqing Ma, and Ke Xu are with State Key Laboratory of Complex & Critical Software Environment, Beihang University, Beihang University, Beijing, China. E-mail: {hujin, xlliu, zhangjunkai, mayuqing, kexu}@buaa.edu.cn. Jin Hu, Xianglong Liu, and Ke Xu are also with Zhongguancun Lab.  
 • Jiakai Wang and Xianqi Yang are with Zhongguancun Lab, Beijing, China. E-mail: {wangjk, yangxq}@mail.zgclab.edu.cn.  
 • Haotong Qin is with ETH Zurich, E-mail: haotong.qin@pbl.ee.ethz.ch

Corresponding author: Xianglong Liu.

efficiency. On the contrary, we define scene-aware and real-time generated PAEs as **dynamic PAEs**, which is a problem that has yet to be addressed in the field. Related attempts are limited to determining patch locations only [21], simulated control of a few states [22], optimization for each clustered scene in the lab [23], and resisting dynamic fluctuations [24] rather than enabling dynamic responses.

This work focuses on overcoming the core challenge, *i.e.*, the key inherent uncertainty of PAEs, of dynamic PAE generation. It is a new generative task that takes the observation from the attacker as the input and the corresponding PAE as the output. However, compared to conventional generative tasks that learn from existing data, this task requires creating unknown adversarial data that is effective in the uncertain world, and the following challenges stem from modeling the *inherent uncertainty* of the PAE generation task need to be tackled: ① Training the dynamic PAE generator is difficult, presented as optimization degeneracy and infinite gradients. The difficulty arises from the noisy gradient feedback [25] in attack training that hinders the exploration of the potentially sparse distributions [26] of PAEs, and the noise originates from the necessary randomness injected into PAE training. ② The real-world attack scenario contains agnostic properties, including incomplete observations that limit the perception of the generator and different attack targets that influence the balance between objectives. Therefore, further modeling of scene-aware attacks is required to eliminate the physical-digital gap and balance the objectives for consistent generative behavior.

To address the dynamic PAE generation problem, we present the DynamicPAE framework that effectively addresses the challenges. As shown in Figure 1, the framework trains the scene-aware generator in the end-to-end paradigm and significantly improves the attack performance under varying conditions. Specifically, to address the training problem that arises from noisy gradients, **residual-driven sample trajectory guidance** is proposed by breaking the limited feedback information restriction that leads to the degeneracy problem. Inspired by deep residual learning [27], we present the construction of the residual task that redefines the optimization problem, enriches the guidance information by relaxing the training with a low-noise auxiliary task, and leads the optimization toward exploring more aggressive results in the sparse space of PAEs. A regularized latent encoding is further proposed to stabilize the exploration. To adapt the agnostic attack scenarios, **context-aligned scene expectation simulation** is proposed. Specifically, the conditional-uncertainty-aligned data module is proposed to inject the randomness that is aligned with the real-world uncertainty, including the uncertainty of incomplete observation, and the skewness-based weight controller is proposed to automatically align the objectives when directly adapting the framework to agnostic target models. By solving the key training and task modeling issues, the framework bridges the gap between generative neural networks and dynamic PAE generation.

We construct a comprehensive digital benchmark on patch attacks, an example of simulated adversarial testing in the autonomous driving scenario, and a physical-world attack prototype system for object detection to evaluate the proposed framework and demonstrate its effectiveness. Our

contribution is summarized as follows:

- We propose the novel dynamic physical adversarial example (PAE), that is generated conditioned on the observation from the attacker in real-time. We propose the DynamicPAE framework that opens the end-to-end modeling of this widely impactful task.
- We propose the *residual-driven sample trajectory guidance* technique, which addresses the degeneracy and instability problem in the generative training of dynamic PAEs. We recognize that the problem arises from the noisy gradient feedback of attack training, and our technique breaks the limited feedback information restriction, which leads to the degeneracy problem, by redefining the training task and allowing the gradient feedback to be passed to the generator through a low-noise auxiliary task. It guides the optimization away from degenerate solutions, leading to a more comprehensive and stable exploration of feasible PAEs.
- We propose the *context-aligned scene expectation simulation* process for addressing the agnostic nature of attack scenarios. It consists of the conditional-uncertainty-aligned data module that improves the robustness under incomplete observations by utilizing domain randomization through the conditional probabilistic model, and the skewness-aligned objective re-weighting module that enables consistent stealthiness control across different attack targets by automatically re-weighting losses using the skewness indicator.
- Extensive experiments across diverse settings demonstrate the superiority of DynamicPAE, *i.e.*, **1.95 $\times$**  of *average AP drop after attack* compared to existing PAEs and **12ms inference latency**. Evaluations on the simulation platform (*i.e.*, CARLA) and physical-world-deployed devices further validate the effectiveness of our proposed method.

The rest of this paper is organized as follows: section 2 presents the background and the definition of the dynamic PAE problem. Section 3 introduces the key components of the DynamicPAE framework. Section 4 details the experimental evaluation, including the settings, the results, and the analysis. Section 5 discusses the related works of the dynamic attack problem and optimization techniques, and section 6 concludes the paper with possible future works.

## 2 PRELIMINARIES

### 2.1 Backgrounds

**Adversarial Examples (AEs)** are a type of specially designed data for fooling deep-learning models [28]. Formally, given a visual recognition model  $\mathcal{F}$ , a benign input  $x$ , and its corresponding ground truth  $y$ , the AE  $\delta$  is designed to satisfy:

$$y \neq \mathcal{F}(x \oplus \delta), \quad \|\delta\|_p \leq \varepsilon, \quad (1)$$

where  $\|\cdot\|_p$  indicates the distance metric under the  $p$ -norm and could be replaced by other metrics,  $\varepsilon$  is a small constant that controls the magnitude of the adversarial attack.

For the AEs to reveal real vulnerabilities, a key issue is whether AEs retain validity in the physical world. In the presence of diverse observations of the physical world by

intelligent models & systems, effective PAEs need to overcome the perturbation to manipulate the target model. This significantly reduces the attack success rate of typical AEs, especially for potent AEs that are iterative optimized [18]. Currently, the key method is to simulate the physical world with the *Expectation over Transformation (EoT)* [29] paradigm to reflect physical world randomness [30]. Also, randomness injection, or domain randomization, is crucial in constructing reality simulation models [31] that prevent the optimizer from exploiting the sim-to-real error of the simulator [32].

In the past decade [33], algorithms supporting PAE generation have mainly focused on applying the iterative optimization with *EoT* paradigm to find a universal PAE that is robust under all simulated scenes [20], [24], [34]–[36]. On the contrary, the solutions based on the inference of non-iterative models, *e.g.*, conditional generative networks [37], have been validated only in the digital or randomness-free scenarios. However, the iterative paradigm does not support scene-adaptive PAEs because it requires inefficient repetitive optimization [9], [38]. It is difficult to fully achieve the capability to present the corresponding PAE by current observation, *i.e.*, *scene-aware*, for the attackers.

In terms of specific tasks, a typical PAE is patch-form [39]–[41], and object detection models are often employed for evaluating the PAEs [17], [42], [43]. This task is not easy since current detection models are well-optimized.

## 2.2 Definitions

Next, we present the key problem definition, and the key notations are provided in Table 1. For attacks in the dynamic and physical worlds, the key difference is the uncontrollable nature of the attack process and the limited perceptibility of the surrounding environment. We formulate the attack scene as the current state of the world  $\mathbf{X} \in \mathbb{X}$ , the transformation parameters  $\theta \in \Theta$  of the attack injection operation  $\oplus$ , and the input obtained by the attacker containing *limited information* about  $\mathbf{X}$  and  $\theta$ , denoted as the physical context data  $\mathbf{P}_X \in \mathcal{P}$ . To achieve practical *real-time* generation, we focus on the challenge of constructing  $\mathcal{G}$  as a generative neural network that models the mapping from the physical observation  $\mathbf{P}_X$  and the corresponding physical AE  $\delta$ . The problem is formulated as follows.

**Definition 2.1.** *The dynamic physical adversarial attack problem is defined as finding a PAE generator  $\mathcal{G}$  that maps the observed physical context data  $\mathbf{P}_X \in \mathcal{P}$  into the PAE  $\delta \in \mathbb{D}$ , formulated as:*

$$\text{find } \mathcal{G} \text{ s.t. } \mathcal{F}(\mathbf{X} \oplus (\mathcal{G}(\mathbf{P}_X), \theta)) \in \mathcal{Y}_{adv}, \quad (2)$$

where  $\mathcal{Y}_{adv}$  is the range of successful attacks defined with the result of victim model(s)  $\mathcal{F}$ ,  $\oplus$  is the attack injection operation that updates the state of the world  $\mathbf{X} \in \mathbb{X}$  with the PAE  $\delta = \mathcal{G}(\mathbf{P}_X)$ , and  $\mathcal{G}$  is the PAE generating network or the iterative algorithm.

## 3 METHODOLOGY

The overview of the DynamicPAE framework is shown in Figure 2. We aim to establish an end-to-end framework for dynamic PAE generation based on the unified representation learning paradigm, which formulates the architecture of the neural PAE generator as follows.

**Table 1: Glossary of Key Notations.**

Notation	Description
$\delta$	Physical Adversarial Example (PAE)
$\mathcal{G}; \mathcal{F}$	Dynamic PAE Generator; victim/target model
$\mathbf{X}; \mathcal{X}$	State of the world; training dataset
$\mathbf{P}_X; \mathcal{P}$	Observation of $\mathbf{X}$ ; range of variable $P$
$\mathcal{Y}$	Range of $\mathcal{F}$ 's output;
$\mathcal{Y}_{adv}$	Range of successful attacks in $\mathcal{Y}$
$\mathbf{Z}; \mathcal{Z}$	Latent embedding; latent space
$\oplus; \theta$	Attack injection operation; parameter of $\oplus$
Enc; Dec	Encoder network; decoder network
$H; I$	Shannon entropy; mutual information
skewness( $\cdot$ )	Skewness statistic
$\lambda$	Sample-wise loss weight, encoded into $\mathcal{G}$
$\alpha$	Task-wise loss weight
$\mathcal{L}_\lambda$	Residual fusion operator parameterized by $\lambda$
$\mathcal{L}_{Atk}; \mathcal{L}_{Inv}$	Attack loss; invisibility loss;
$\mathcal{L}_{Reg}$	Regularization loss
$\mathcal{L}_{GCAtk}$	<i>Guided and Controlled Attack Loss</i>

**Definition 3.1** (Neural PAE Generator). *The PAE generation module  $\mathcal{G}$  is defined by the unified representation learning paradigm as:*

$$\mathcal{G} := \text{Dec} \circ \text{Enc}, \text{ Enc} : \mathcal{P} \rightarrow \mathcal{Z} \subseteq \mathbb{R}^d, \quad (3)$$

where  $\mathcal{Z}$  is the space of latent representation, and Enc and Dec are the encoder and the decoder, respectively.

To enable effective training of the PAE generator  $\mathcal{G}$ , the framework synergizes two key components: residual-driven sample trajectory guidance to tackle the training difficulties arise from noisy gradient feedback; and context-aligned scene expectation simulation to adapt to agnostic attack scenarios, including incomplete observations and agnostic attack targets, thereby achieving the dynamic adversarial attack in the real world.

### 3.1 Residual-Driven Sample Trajectory Guidance

Training the dynamic PAE generator faces the challenge of noisy gradient feedback, which leads to the degeneracy and instability problem of the generative training (shown in the experiments in section 4.3.1). To analyze the training problem, we bridge the *noisy gradient* model and the *sample trajectory* analysis with the *limited feedback information restriction* and recognize that the necessary randomness injected in the PAE optimization task leads to the training degeneracy of the dynamic PAE generator. Inspired by deep residual learning, we tackle the problem by constructing a residual task that relaxes the original attack training and breaks the *limited feedback information restriction*. We further propose the additional regularization of the latent encoding to tackle the *latent evasion* problem related to the unconventional gradient property and stabilize the training. Afterward, the training escapes from degenerate solutions and allows a more stable and comprehensive exploration of feasible PAEs.

- **Analysis of the Degeneracy:** Previous works have demonstrated that *obfuscated gradient* [25] is a mechanism of adversarial defense techniques and adaptive attacks shall overcome it [44]. Section 4.3.1 provides compelling evidence that the simulated transformation has a similar impact on

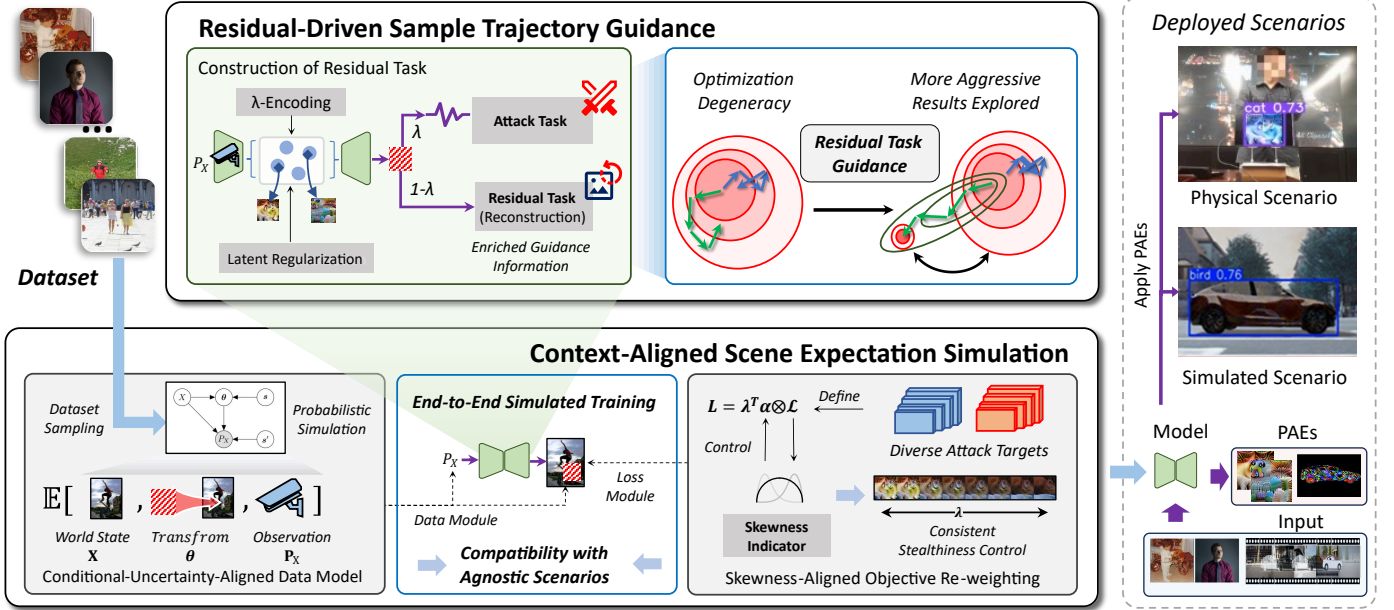


**Figure 2: The overview of the DynamicPAE framework proposed for the dynamic physical adversarial attack problem.** The framework establishes the training paradigm of *Residual-Driven Sample Trajectory Guidance* that solves the training difficulties arise from noisy gradient feedback, and the *Context-Aligned Scene Expectation Simulation* that adapts the model to agnostic scenarios.

PGD optimization, confirming the existence of the noisy gradient problem. Intuitively, a small distortion in the environment ( $\mathbf{X}, \theta$ ) may cause the gradient feedback of the attack task  $\nabla_{\delta} \mathcal{L}_{\text{Atk}}$  changes significantly. We formulate the **limited feedback information restriction** to model the problem based on the mutual information and entropy metrics on  $\nabla_{\delta} \mathcal{L}_{\text{Atk}}$  and the (bottleneck) latent variable  $\mathbf{Z}$ :

$$I(\nabla_{\delta} \mathcal{L}_{\text{Atk}}; \mathbf{Z}) / H(\nabla_{\delta} \mathcal{L}_{\text{Atk}}) < \epsilon, \quad (4)$$

indicating that the uncertainty of  $\nabla_{\delta} \mathcal{L}_{\text{Atk}}$  is significantly higher than the uncertainty in  $\nabla_{\delta} \mathcal{L}_{\text{Atk}}$  reduced by  $\mathbf{Z}$ .

We then analyze the sample trajectory with this model to understand the optimization degeneration problem. Specifically, considering the gradient descent process of deep learning, the trajectory of the generated PAEs  $\delta$  in training step  $t$  can be modeled by:

$$\begin{aligned} \delta^{(t+1)} &= \delta^{(t)} + \eta \nabla_{\delta} \mathcal{L}_{\text{Atk}}^{(t)}, \\ \nabla_{\delta} \mathcal{L}_{\text{Atk}}^{(t)} &= f^{(t)}(\mathbf{Z}, \delta) + g^{(t)}(\delta), \end{aligned} \quad (5)$$

where  $\eta$  is the learning rate,  $g^{(t)}$  is the noise introduced by random simulated transformation, and the term  $f^{(t)}$  is the components correlated with  $\mathbf{Z}$ , representing the learnable information. By *rate-distortion theory*, the signal power  $\mathbb{E}[|f^{(t)}|^2]$  is significantly lower than the noise power  $\mathbb{E}[|g^{(t)}|^2]$  if  $I(\nabla_{\delta} \mathcal{L}_{\text{Atk}}; \mathbf{Z})$  is relatively small according to Eq. 4. Based on the empirical fact of the existence of universal AE [45], the AE optimization contains isotropic components, and  $\mathbb{E}[g^{(t)}]$  is large. Thus the optimization of PAE may converge to the local minimum determined by  $g^{(t)}$  and  $\mathbb{E}[g^{(t)}]$  even with sufficient large steps  $t$ , which is coherent with the experiment results in section 4.3.1.

This result indicates the hardness of SGD optimization in learning PAEs and is independent of whether the optimizer

includes techniques like momentum to escape from local optima. Generative models, especially single-step models such as *GAN*, have long faced the similar experimental challenge of mode collapse in the manifold sampling tasks, in particular on disconnected manifolds [46]–[48]. Rather than relying on generative model construction techniques, we propose a task-driven approach and formulate solutions that are well-suited to the problem itself.

• **Optimization Guidance with Residual Task:** Inspired by deep residual learning [27], we bypass this difficulty by redefining the optimization task. Specifically, we simply relax the adversarial attack task with the additional task  $\mathcal{R}$  with the conditional parameter  $\lambda$ , and modify the loss from  $\mathcal{L}_{\text{Atk}}(\delta(\cdot))$  to  $\mathcal{L}_{\lambda}(\mathcal{L}_{\text{Atk}}, \mathcal{L}_{\mathcal{R}})$ , defined as:

$$\mathcal{L}_{\lambda}(\mathcal{L}_{\text{Atk}}, \mathcal{L}_{\mathcal{R}}) := \lambda \mathcal{L}_{\text{Atk}}(\delta(\cdot, \lambda)) + (1 - \lambda) \mathcal{L}_{\mathcal{R}}(\delta(\cdot, \lambda)), \quad (6)$$

We denote  $\mathcal{L}$  as the *residual fusion* operator. The modification aims to break the noisy gradient model in Eq. 4 by constructing  $\mathcal{L}_{\mathcal{R}}$  to be more dependent on the learnable latent representation:

$$\exists \lambda \text{ s.t. } I(\nabla_{\delta} \mathcal{L}_{\lambda}(\mathcal{L}_{\text{Atk}}, \mathcal{L}_{\mathcal{R}}); \mathbf{Z}(\cdot, \lambda)) \gg I(\nabla_{\delta} \mathcal{L}_{\text{Atk}}; \mathbf{Z}). \quad (7)$$

Afterward, the imbalanced noise issue in SGD optimization is solved, which mitigates the occurrence of degeneration. Further, the optimal PAE solution remains identical when  $\lambda = 0$ . Since the gradient takes a noiseless path, or a residual path, to the parameters of  $\mathcal{G}$ , we identify task  $\mathcal{R}$  as the *auxiliary residual task*.

More intuitively, the goal of the residual task in generating PAEs is to encourage the exploration of the global space of PAEs. Inspired by the construction of the denoising task in diffusion models to learn the entire gradient field [49], we designate local area reconstruction as the auxiliary residual task  $\mathcal{R}$  ( $\mathcal{L}_{\mathcal{R}} := \mathcal{L}_{\text{Inv}}$ ) since it is directly related to the

model input, is well studied by generative models, and lets the model learns to generate PAEs at different magnitudes, possessing the utility of *controllable stealthiness*. Specifically, we adapt the mean square error (*MSE*) as the objective quality metric and the *LPIPS* [50] as the subjective quality metric, and integrate them as:

$$\mathcal{L}_{\text{Inv}} := \text{MSE}(\mathbf{X}, \mathbf{X}') + \text{LPIPS}(\mathbf{X}, \mathbf{X}'). \quad (8)$$

where  $\mathbf{X}$  and  $\mathbf{X}' = \mathbf{X} \oplus \boldsymbol{\delta}$  is the global image capture before and after applying PAE  $\boldsymbol{\delta}$ , respectively.

To enable diverse sampling of  $\lambda$  during training, the magnitude of attack objectives for each batch of data  $\boldsymbol{\lambda} = [\lambda_1, \lambda_2, \dots, \lambda_b]$  is sampled by the distribution:

$$\lambda_i \sim \begin{cases} \delta(0) & i \in [1, b/4] \\ \delta(1) & i \in (b/4, b/2] \\ \mathcal{U}(0, 1) & i \in (b/2, b] \end{cases} \quad (9)$$

where  $\delta$  denotes the Dirac distribution and  $b$  denotes the batch size. The distribution is constructed by sampling minimal, maximal, and random hyper-parameters and is inspired by the sampling techniques in auto-ML training [51]. To generate PAEs conditioned on  $\lambda$ ,  $\lambda$  is encoded into the latent representation  $\mathbf{Z}$  in  $\mathcal{G}$  by log embeddings and a MLP module modeling the non-linear transformation:

$$\mathbf{Z}' = \text{MLP}(-\log(\max\{\lambda, \exp(-10)\}) + \mathbf{Z}. \quad (10)$$

Afterward, the generator  $\mathcal{G}$  generates PAEs with conditioned magnitude  $\boldsymbol{\delta} = [\delta_{\lambda_1}, \delta_{\lambda_2}, \dots, \delta_{\lambda_b}]$  in each batch, and the same  $\boldsymbol{\lambda}$  is applied to Eq. 6 as training objectives.

- **Stabilizing Sample Exploration:** The particularity of the dynamic PAE generation also exists in the latent space of generator  $\mathcal{G}$ . Empirically, we observed a non-trivial gradient explosion behavior in the generator during training. The analysis is shown in section 4.3.2 and the supplementary material, indicating the difference between PAE generation and conventional tasks. We recognize it as the **latent evasion** problem, which stems from the process of exploring PAEs.

Specifically, due to the analyzed noisy gradient problem, the discovery of new conditional PAEs often requires multiple steps of fitting to emerge. Meanwhile, the disentangled representations and weights within the model continuously deviate towards a certain direction throughout the multi-step fitting process, causing their norms to continually increase. Furthermore, the overall discontinuity of the PAE distribution further intensifies this phenomenon. Therefore, the optimization speed of the model's internal representations should be slowed down. Thus, to tackle this problem, we incorporate a regularization loss on the latent representation of PAEs  $\mathbf{Z}$  to stabilize the exploration, which together regularizes the PAEs with the total variation loss  $\mathcal{L}_{\text{TV}}$  [52] on the data space that eliminates the frequency discrepancy between PAEs and physical realizable images:

$$\mathcal{L}_{\text{Reg}} := \gamma \cdot \|\mathbf{Z}\|_2^2 + \beta \cdot \mathcal{L}_{\text{TV}}, \quad (11)$$

where  $\gamma$  is the hyper-parameter. Note that the latent regularization is more like *BatchNorm*, which aims at tackling the optimization difficulties rather than preventing overfitting. We further compare the regularization with the classical VAE prior in experiments.

### 3.2 Context-Aligned Scene Expectation Simulation

The practical PAE methods should be compatible with the variable and agnostic scenario. For the dynamic attack scenarios, the critical issues are incomplete observations from the attacker, which limit the perception of the generator, and the agnostic nature of target models and tasks, which affect the balance between objectives. To bridge the gap between the training environment and potential deployment scenarios, firstly, we propose the conditional-uncertainty-aligned data module. This module allows the generator to accommodate incomplete observations by employing a conditional probabilistic model for domain randomization. Secondly, we propose the skewness-aligned objective re-weighting module, which uses the skewness indicator to balance multiple optimization objectives, including stealth and aggressive, under agnostic attack targets. Thus, consistency in the sampling and control of stealth and attack objectives is maintained, and hyper-parameter tuning is eliminated.

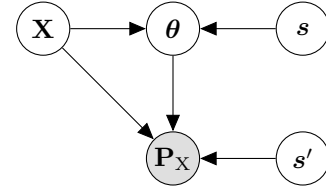


Figure 3: Conditional Probabilistic Model Generating Dynamic Physical Adversarial Attack Scenes

- **Conditional-Uncertainty-Aligned Data Model:** We align the training and real-world scenes by creating a conditional probabilistic model to generate the incomplete observation  $\mathbf{P}_X$ , as illustrated in Figure 3, based on the dynamic attack problem formulation in Equation 2. In this model, the parameters  $\boldsymbol{\theta}$  of the attack injection process are generated by the current state of the world  $\mathbf{X}$  and a random factor  $s$ , which, along with  $\mathbf{X}$  and another random factor  $s'$ , jointly generate the physical context data  $\mathbf{P}_X$  that the attacker acquires. The training is performed by minimizing the expected losses under the data model, where  $\Omega$  and  $\Theta$  are the probability distribution that generates  $\mathbf{P}_X$  and  $\boldsymbol{\theta}$ , respectively:

$$\min \mathbb{E}_{\mathbf{P}_X \sim \Omega(\boldsymbol{\theta}, \mathbf{X}), \boldsymbol{\theta} \sim \Theta(\mathbf{X}), \mathbf{X} \sim \mathcal{X}} [\mathcal{L}(\mathcal{F}(\mathbf{X} \oplus (\mathcal{G}(\mathbf{P}_X), \boldsymbol{\theta})))], \quad (12)$$

where  $\mathcal{L}$  is the total loss function, which is defined as  $\mathcal{L}_{\text{Total}}$  in the following context. For patch attacks, the attack injection  $\oplus$  is formulated as:

$$\mathbf{X} \oplus (\boldsymbol{\delta}, \boldsymbol{\theta}) := \mathbf{X} \otimes (1 - \mathbf{m}_{\boldsymbol{\theta}}) + \text{AffineTransform}(\boldsymbol{\delta}, \mathbf{A}_{\boldsymbol{\theta}}) \otimes \mathbf{m}_{\boldsymbol{\theta}}, \quad (13)$$

where the binary mask  $\mathbf{m}_{\boldsymbol{\theta}} \in \{0, 1\}^{H_1 \times W_1}$  representing the configurable patch location corresponding to  $\boldsymbol{\theta}$ . Considering the input of the attack device, the local feature corresponding to the stealthiness and the global context corresponding to the aggressiveness are included in  $\mathbf{P}_X$ , as the attack objective is correlated with the global attention field of the model [53]. Specifically, the local feature is introduced by the local image content  $\mathbf{X}_{\text{local}} \in \mathbb{R}^{H_2 \times W_2 \times 3}$  around the patch, while the global context corresponds to a global

image  $\mathbf{X}_{global} \in \mathbb{R}^{H_1 \times W_1 \times 3}$  representing the observed environment. To simulate the distortion in the open world, the *RandAugment* [54] method is applied to  $\mathbf{X}_{global}$  and  $\mathbf{m}_\theta$  simultaneously. *Las Vegas algorithm* is performed to ensure the physical validity: the augmentation pipeline reruns if the result is invalid. Thus, the distribution  $\Omega$  that generates  $\mathbf{P}_X$  is formulated as:

$$\Omega(\theta, \mathbf{X}) = [\mathbf{X}_{local}; RandAug(\mathbf{X}_{global}, \mathbf{s}'); RandAug(\mathbf{m}_\theta, \mathbf{s}')], \quad (14)$$

where  $\mathbf{s}'$  is the generated random seed for *RandAugment*.  $\Theta$  is constructed by sampling the object location according to the objects in  $\mathbf{X}$ , and  $\mathbf{X}$  is constructed by the training dataset of the target model.

• **Skewness-Aligned Objective Re-weighting:** The dynamic PAE generator may be deployed to evaluate and attack diverse victim models and corresponding tasks. To balance the stealth and attack objectives, achieve controllable stealthiness, and avoid manual adjustment of the optimization-related parameters when facing new targets, we further propose an objective re-weighting approach based on the *skewness* measurement [55]. Specifically, we first focus on adding and determining the additional relative weights  $\alpha \in (0, 1)$  of the *residual task*, and define the optimization objective using the *residual fusion* operator in Eq. 6 as:  $\mathcal{L}_\lambda((1-\alpha)\mathcal{L}_{Atk}, \alpha\mathcal{L}_{Inv}) = \lambda(1-\alpha)\mathcal{L}_{Atk} + (1-\lambda)\alpha\mathcal{L}_{Inv}$ .

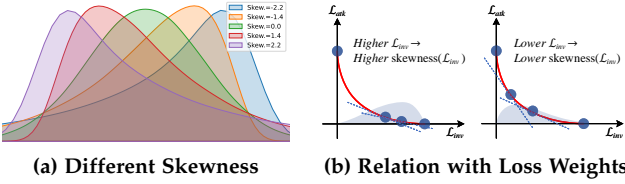


Figure 4: Skewness-based Hyperparameter Control

Intuitively, skewness aims to measure the lack of symmetry in the distribution of a dataset around its mean. On one hand, as shown in Figure 4a, if the skewness is positive, the distribution is right-skewed or positively skewed, and vice versa. On the other hand, as shown in Figure 4b, the  $\mathcal{L}_{Inv}$  of the samples that are generated by middle-size  $\lambda$  tends to decrease within the optimal curve as the weights  $\alpha$  increase, leading to a decrease in the loss skewness. This allows for the skewness to be utilized as an indicator variable to control the value of  $\alpha$  by measuring the distribution of losses. Thus, based on the skewness of the loss values, we define the gradient feedback of the  $\alpha$ -controller of loss  $\mathcal{L}$  as:

$$\nabla\alpha := -\text{skewness}(\mathcal{L}_{Inv}) + \varsigma, \quad (15)$$

$$\text{skewness}(\mathcal{L}_{Inv}) := \mathbb{E}\left[\frac{(\mathcal{L}_{Inv} - \mu(\mathcal{L}_{Inv, \lambda=0,1}))^3}{\sigma(\mathcal{L}_{Inv, \lambda=0,1})^3}\right],$$

where  $\varsigma$  is the target skewness,  $\mu$  and  $\sigma$  are the mean and standard deviation of the loss when  $\lambda \in \{0, 1\}$ , which replaces the statistics for all samples for better stability. The gradient  $\nabla\alpha$  equals zero if and only if the loss is balanced, that is,  $\text{skewness}(\mathcal{L}) = \varsigma$ . For implementation, we re-parameterize  $\alpha$  as  $\alpha = e^\beta \in (0, +\infty)$  and optimize  $\beta$  using Adam optimizer. We set the target skewness of the reconstruction loss  $\mathcal{L}_{Inv}$  to zero ( $\varsigma = 0$ ), and the estimation

of  $\mu$  and  $\sigma$  is performed by the moving average. The convergence of the controller is shown by the following proposition, and the proof is given in the *supplementary material* by analyzing the trade-off curve.

**Proposition 3.1.**  $\nabla^2\alpha < 0$  if  $\mathcal{L}_{Atk}$  is strictly negatively correlated to  $\mathcal{L}_{Inv}$  for any set of measured PAEs  $\delta_\lambda$  that are optimal for the overall optimization objective  $\mathcal{L}$  under a certain value of  $\lambda$ .

We further generalize our framework to the multi-objective attack scenario, consisting of  $t$  attack and residual tasks. The losses of these tasks are composed by the sample-wise loss weights  $\lambda = [\lambda_1, \lambda_2, \dots, \lambda_b] \in \mathbb{R}^{b \times t}$ , which are encoded into  $\mathcal{G}$ , and task-wise loss weights  $\alpha \in (\mathbb{R}^+)^t$ , which are controlled by the skewness indicator and satisfy  $\sum_{i=1}^t \alpha_i = 1$ . We define the composed loss as the *Guided and Controlled Attack Loss*  $\mathcal{L}_{GCAtk}$ :

$$\mathcal{L}_{GCAtk} := \sum_{i=1}^b \sum_{j=1}^t \{\lambda \alpha^T \otimes \mathbf{L}\}_{i,j}, \quad (16)$$

where  $\otimes$  denotes the Hadamard product,  $t$  is the number of tasks,  $b$  is the batch size, and  $\mathbf{L} \in \mathbb{R}^{b \times t}$  is the loss matrix of  $t$  tasks and  $b$  items in a batch defined by the attack scenario with  $\mathcal{L}_{Atk}$ . For the single-objective adversarial attack implementation,  $t = 2$  and  $\mathbf{L} = [\mathcal{L}_{Atk}, \mathcal{L}_{Inv}]$ , and in this case:

$$\mathcal{L}_{GCAtk} = \mathcal{L}_\lambda((1-\alpha)\mathcal{L}_{Atk}, \alpha\mathcal{L}_{Inv}). \quad (17)$$

For the attack loss  $\mathcal{L}_{Atk}$ , we implement it according to the specific scenario in experiments.

• **Training and Deployment Pipeline:** By aligning the training environment and deployment environment, we can establish an *end-to-end* pipeline for building dynamic PAE generator. For the overall training, the total loss is formulated as:

$$\mathcal{L}_{Total} = \mathcal{L}_{GCAtk} + \mathcal{L}_{Reg} + \mathcal{L}_{VAE}, \quad (18)$$

where  $\mathcal{L}_{Reg}$  is the regularization loss in Eq. 11. We also incorporate an auto-regressive training loss  $\mathcal{L}_{VAE}$  with  $\beta$ -VAE [56] with images from the dataset  $\mathcal{X}$  to train Enc and let  $\mathcal{G}$  maintain the modeling capability of more complex natural images. The training pipeline is performed by simulating the physical observation  $\mathbf{P}_X$  and sampling  $\lambda$ , generating PAEs  $\delta$  based on it, evaluating the losses, and performing optimization on model parameters by  $\nabla\mathcal{L}_{Total}$  and on  $\alpha$  by Eq. 15. We deploy the generator directly on edge devices after training and achieve real-time generation by connecting it with the camera and display. Detailed training implementation is shown in the *supplementary material*.

## 4 EXPERIMENTS

We evaluate our framework in both digital and physical environments on the object detection task since it is classical for both physical and digital attacks. The experiments are conducted in the following aspects: ① The performance of our model in the benchmark. ② The analysis corresponds with the methodologies that tackle the challenge of noisy gradient feedback in PAE generator training and the agnostic nature of attack scenarios. ③ The ablation of the key components.

## 4.1 Experiment Settings

In this subsection, we describe the key settings of the experiments. We use the COCO [57] and the Inria [58] as the dataset of the person detection task, while data collected from CARLA is used for the simulation experiment. Detailed *attack transformation*, *method implementation*, *dataset description*, and *victim model description* are shown in the *supplementary material*.

**Metrics:** The average precision (AP), formulated as follows by the precision  $Pre(c)$  and recall  $Rec(c)$  of confidence threshold  $c$  is applied as the metric of adversary performance.

$$AP = \int_{r=0}^1 \max_c Pre(c) \cdot [Rec(c) \leq r] dr \in [0, 1]. \quad (19)$$

We adopt two confidence thresholds: the first is  $c_{min} = 50\%$ , with the corresponding metric denoted as  $AP_{50}$ , which serves as the evaluation metric identical to the practice of previous object detection attack evaluation. The second threshold is  $c_{min} = 1\%$ , with the metric denoted as  $AP_{01}$ , as a more stringent evaluation metric. All  $iou$  thresholds are set as 0.5. The low-confidence and unattacked bounding boxes are filtered out during post-processing.

To ensure fairness, we use *consistent* patch placement parameters in the evaluation to control the overall stealthiness of the attack. Some specific methods also have other factors affecting stealthiness, such as the naturalness constraint of GAN-NAP, so we additionally assessed relevant metrics in the experiment. We use the Structural Similarity Index (SSIM) and the Learned Perceptual Image Patch Similarity (LPIPS) as metrics to measure the stealthiness of the patches. Both SSIM and LPIPS have a range of  $[0, 1]$ . *SSIM is not included as a loss during the training of our model.*

**Table 2: Comparison of different baselines.**

Baselines	PGD	AdvGAN	T-SEA	GAN-NAP
DNN based	✗	✓	✗	✓
Physical Capability	✓	✗	✓	✓
Adaptive	✓	✓	✗	✗
Patch Attack	✓	✗	✓	✓
Perturbation	✓	✓	✗	✗

**Baseline Attack Methods:** For the novel task of dynamic attack, we select representative methods as baselines and adapt them to the test setup including PGD [59], AdvGAN [37], GAN-NAP [42], also known as NAP, and T-SEA [43]. The comparison of these methods is shown in Table 2. PGD, GAN-NAP, and T-SEA are adapted as patch-form PAE evaluation baselines. For the simulated experiment, we conducted supplementary evaluations on similar AdvGAN methods. For the physical experiment, we performed tests using existing patch attacks (GAN-NAP and T-SEA).

**Attack Method Implementations:** Unlike training universal adversarial patch, dynamic PAE training requires the model to learn spatial correlations, thus a selection of bounding boxes (Bboxes) is needed. For loss construction, the maximum confidence value is employed following GAN-NAP with the addition of a selection mask:

$$\mathcal{L}_{Atk} = \|\mathbf{conf} \cdot [iou > 0.3]\|_\infty, \quad (20)$$

where  $iou$  is calculated between the generated and target Bboxes. The detailed implementation is provided in the *supplementary material*.

## 4.2 Performances Evaluation

We evaluate performance based on settings similar to classical PAE studies [39] to focus on comparing PAE optimization or learning methods instead of the simulation. Furthermore, the stealthiness metrics are included to enhance the fairness for biased optimization.

We trained our model on the COCO dataset only and others on data identical to the evaluation datasets. The trade-off between the attack performance and the distortion of the original image is shown in Figure 5, demonstrating the significantly superior attack-distortion curve. Since our model can perform generation conditioned on  $\lambda$  and automatically balance the attack and invisibility by the *Skewness-Aligned Objective Re-weighting* method, the curve in each sub-graph is evaluated in just one training session with the test-time settings of  $\lambda = \{0.0, 0.1, 0.2, \dots, 1.0\}$ . However, the static PAE methods are only able to produce a single result, and thus our model achieves better practicality in PAE-driven model evaluation. The numerical results are shown in Table 3, presenting the setting of  $\lambda = 0.8$  of *DynamicPAE*, which is generally more stealthy according to the attack-distortion curve. It is distinct that the dynamic PAE generated by our model achieves better performance, *i.e.*, lower  $AP_{50}$  and  $AP_{01}$  values. Specifically,  $DynamicPAE_{\lambda=0.8}$  boost the average drop of  $AP_{50}$  to  $-65.55\% (1.95 \times$  on average) while preserving comparable stealthiness measured by SSIM, and only under one configuration (Yolov5-m, Inria) can T-sea achieve comparable aggressiveness. Furthermore, our model achieves  $1.3 \times$  of  $AP_{50}$  average drop compared to performing PGD on each image. In particular, for models with larger parameter sizes (Yolov3-m and Faster-RCNN), our approach exhibits more significant attack performance superiority, suggesting that our model can be scaled up for evaluating the adversarial robustness of larger-scale models. Furthermore, our method has not been trained on the Inria dataset, so the successful attacks on the Inria dataset indicate the zero-shot generalization capability in applying to proprietary data. We evaluate more transformation settings in the *supplementary material* and have the same result, except PGD performs better in zero spatial transformation.

We acknowledge that with a sufficiently large number of iterations, attacks based on traditional optimization, represented by PGD, under the same parameter distribution of  $\oplus$  and the same image  $X$  may be able to achieve better attack results, but at an unacceptable time overhead. We present a comparison of time consumption in Table 4. All of the training and validation except  $DynamicPAE_{Inf.}$  is done on one Nvidia A40 with bf16 enabled.  $DynamicPAE_{Val.}$ ,  $DynamicPAE_{Inf.}$  and PGD are timed through `torch.cuda.Event` after CUDA warmup, and they are tested on the Inria dataset with multiple runs.  $DynamicPAE_{Val.}$  achieves a speedup of more than **2000** times compared to generating the PAE for each image with PGD and maintains higher attack performance.  $DynamicPAE_{Inf.}$  shows that our model can provide real-time patch generation even on personal graphics cards. Moreover, our training time is acceptable (about 40 hours

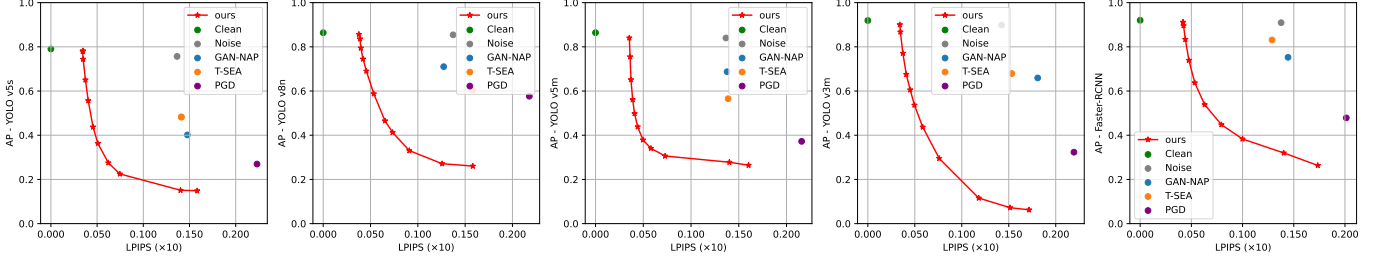


Figure 5: Aggressiveness-distortion curve evaluated on COCO dataset, corresponding to Table 3.

Table 3: Performance Evaluation.  $\downarrow$  indicates smaller values are better, while  $\uparrow$  signifies larger values are preferred. Since the patch size is already constrained, stealthiness is only for better fairness.

Models	Datasets	Method	MSCOCO				Inria			
			AP <sub>50</sub> $\downarrow$	AP <sub>01</sub> $\downarrow$	SSIM $\uparrow$	LPIPS $\downarrow$	AP <sub>50</sub> $\downarrow$	AP <sub>01</sub> $\downarrow$	SSIM $\uparrow$	LPIPS $\downarrow$
Yolov8-n	Clean		0.864	0.921	—	—	0.933	0.941	—	—
	Noise		0.854 $\downarrow$ 1.0%	0.913 $\downarrow$ 0.8%	0.9892	0.0137	0.905 $\downarrow$ 2.7%	0.918 $\downarrow$ 2.3%	0.9950	0.0070
	PGD		0.577 $\downarrow$ 28.7%	0.715 $\downarrow$ 20.6%	0.9883	0.0218	0.577 $\downarrow$ 35.6%	0.644 $\downarrow$ 29.7%	0.9947	0.0133
	T-sea		0.604 $\downarrow$ 25.9%	0.750 $\downarrow$ 17.1%	0.9893	0.0158	0.389 $\downarrow$ 54.3%	0.430 $\downarrow$ 51.1%	0.9953	0.0075
	GAN-NAP		0.710 $\downarrow$ 15.4%	0.810 $\downarrow$ 11.0%	0.9897	0.0127	0.594 $\downarrow$ 33.9%	0.642 $\downarrow$ 30.0%	0.9954	0.0084
	DynamicPAE $_{\lambda=0.8}$		<b>0.331</b> $\downarrow$ 53.3%	<b>0.438</b> $\downarrow$ 48.3%	<b>0.9912</b>	<b>0.0091</b>	<b>0.307</b> $\downarrow$ 62.6%	<b>0.354</b> $\downarrow$ 58.7%	<b>0.9956</b>	<b>0.0069</b>
Yolov5-s	Clean		0.790	0.876	—	—	0.917	0.921	—	—
	Noise		0.757 $\downarrow$ 3.4%	0.848 $\downarrow$ 2.8%	0.9892	0.0137	0.851 $\downarrow$ 6.6%	0.865 $\downarrow$ 5.7%	0.9951	0.0068
	PGD		0.270 $\downarrow$ 52.1%	0.423 $\downarrow$ 45.3%	0.9884	0.0223	0.283 $\downarrow$ 63.4%	0.375 $\downarrow$ 54.6%	0.9948	0.0137
	T-sea		0.482 $\downarrow$ 30.8%	0.631 $\downarrow$ 24.5%	0.9898	0.0141	0.365 $\downarrow$ 55.2%	0.410 $\downarrow$ 51.1%	0.9950	0.0091
	GAN-NAP		0.401 $\downarrow$ 38.9%	0.564 $\downarrow$ 31.2%	0.9893	0.0148	0.352 $\downarrow$ 56.5%	0.433 $\downarrow$ 48.8%	0.9952	0.0086
	DynamicPAE $_{\lambda=0.8}$		<b>0.225</b> $\downarrow$ 56.6%	<b>0.420</b> $\downarrow$ 45.6%	<b>0.9917</b>	<b>0.0075</b>	<b>0.139</b> $\downarrow$ 77.8%	<b>0.256</b> $\downarrow$ 66.5%	<b>0.9955</b>	<b>0.0068</b>
Yolov5-m	Clean		0.864	0.907	—	—	0.920	0.924	—	—
	Noise		0.840 $\downarrow$ 2.4%	0.892 $\downarrow$ 1.5%	0.9892	0.0137	0.837 $\downarrow$ 8.3%	0.848 $\downarrow$ 7.6%	0.9951	0.0068
	PGD		0.372 $\downarrow$ 49.2%	0.488 $\downarrow$ 41.8%	0.9884	0.0216	0.364 $\downarrow$ 55.7%	0.420 $\downarrow$ 50.4%	0.9948	0.0130
	T-sea		0.565 $\downarrow$ 29.9%	0.610 $\downarrow$ 29.7%	0.9900	0.0139	0.350 $\downarrow$ 57.0%	<b>0.372</b> $\downarrow$ 55.1%	0.9953	0.0080
	GAN-NAP		0.687 $\downarrow$ 17.7%	0.772 $\downarrow$ 13.5%	0.9896	0.0138	0.517 $\downarrow$ 40.3%	0.558 $\downarrow$ 36.6%	0.9954	0.0086
	DynamicPAE $_{\lambda=0.8}$		<b>0.306</b> $\downarrow$ 55.8%	<b>0.427</b> $\downarrow$ 47.9%	<b>0.9918</b>	<b>0.0073</b>	<b>0.323</b> $\downarrow$ 59.7%	<b>0.388</b> $\downarrow$ 53.6%	<b>0.9960</b>	<b>0.0049</b>
Yolov3-m	Clean		0.919	0.932	—	—	0.937	0.938	—	—
	Noise		0.898 $\downarrow$ 2.1%	0.914 $\downarrow$ 1.8%	0.9891	0.0142	0.895 $\downarrow$ 4.3%	0.898 $\downarrow$ 4.0%	0.9950	0.0072
	PGD		0.323 $\downarrow$ 59.6%	0.391 $\downarrow$ 54.0%	0.9882	0.0219	0.306 $\downarrow$ 63.1%	0.338 $\downarrow$ 60.1%	0.9946	0.0140
	T-sea		0.679 $\downarrow$ 24.0%	0.728 $\downarrow$ 20.3%	0.9896	0.0153	0.774 $\downarrow$ 16.3%	0.784 $\downarrow$ 15.4%	0.9953	0.0083
	GAN-NAP		0.659 $\downarrow$ 26.0%	0.692 $\downarrow$ 23.9%	0.9893	0.0181	0.640 $\downarrow$ 29.8%	0.663 $\downarrow$ 27.5%	0.9954	0.0108
	DynamicPAE $_{\lambda=0.8}$		<b>0.116</b> $\downarrow$ 80.3%	<b>0.159</b> $\downarrow$ 77.2%	<b>0.9903</b>	<b>0.0118</b>	<b>0.089</b> $\downarrow$ 84.8%	<b>0.124</b> $\downarrow$ 81.4%	0.9950	0.0096
Faster-RCNN	Clean		0.920	0.927	—	—	0.944	0.944	—	—
	Noise		0.909 $\downarrow$ 1.1%	0.916 $\downarrow$ 1.0%	0.9891	0.0138	0.914 $\downarrow$ 3.0%	0.917 $\downarrow$ 2.7%	0.9951	0.0068
	PGD		0.478 $\downarrow$ 44.2%	0.493 $\downarrow$ 43.4%	0.9884	0.0201	0.369 $\downarrow$ 57.5%	0.378 $\downarrow$ 56.6%	0.9948	0.0124
	T-sea		0.831 $\downarrow$ 8.9%	0.844 $\downarrow$ 8.3%	0.9901	0.0129	0.601 $\downarrow$ 34.3%	0.614 $\downarrow$ 33.0%	0.9952	0.0097
	GAN-NAP		0.753 $\downarrow$ 16.8%	0.768 $\downarrow$ 15.8%	0.9900	0.0144	0.834 $\downarrow$ 11.0%	0.839 $\downarrow$ 10.5%	<b>0.9958</b>	<b>0.0057</b>
	DynamicPAE $_{\lambda=0.8}$		<b>0.383</b> $\downarrow$ 53.7%	<b>0.398</b> $\downarrow$ 52.9%	<b>0.9911</b>	<b>0.0100</b>	<b>0.235</b> $\downarrow$ 70.9%	<b>0.244</b> $\downarrow$ 70.0%	<b>0.9953</b>	0.0082

The values bolded indicate the best results, the values underlined indicate the second-best results, the gray cells represent our method, and the subscript values represent the indicator decrease relative to the “Clean”.

on a single GPU). Evaluation of more PGD parameters is shown in section 4.3.1.

Table 4: Evaluation of GPU processing time. PGD and  $DynamicPAE_{Val}$  denote the average time of PAE generation on a batch of images with  $batchsize = 32$ , and  $DynamicPAE_{Inf}$  shows the single-image inference latency. Static PAEs (T-sea and GAN-NAP) do not require inference computation, and thus they are not included.

	Yolov5-s	Yolov8-n	Yolov3-m	Yolov5-m
PGD	288.3s	175.1s	702.5s	451.0s
$DynamicPAE_{Val}$			87.36ms	
$DynamicPAE_{Inf}$			11.910 ms (single image, 2080Ti)	

### 4.3 On Overcoming the Noisy Gradient in PAE Training

Existing works have shown the special characteristics of AEs and the adversarial attack problems, including its physical robustness [18], distributional properties [26], [60], [61], and gradient properties of the optimization process [25]. For the dynamic PAE training, we identify the key challenge as the *noisy gradient problem*, causing the problem of *degenerated solution* and *latent evasion* in the generative training, which can be regarded as originating from the necessary randomness injected into PAE training. To illustrate the challenge and evaluate the effectiveness of the proposed model and solution, we analyze each problem and our corresponding solution in terms of gradients and sample/latent space.

### 4.3.1 Analysis and Solving the Noisy Gradient Problem

**Obfuscated Gradient Perspective:** Obfuscated Gradient [25] is recognized as a typical defense mechanism in digital adversarial attacks since the defenders could significantly increase the difficulty of performing gradient descent optimization by adding random transformation. The solution for the attack is applying multiple-step attacks, or EoT, which is also a key algorithm for PAE [29] since the fluctuation in the physical world can be regarded as naturally introduced randomness.

First, we show that the simulated physical adversarial patch attacks, as a typical physical attack, can be regarded as facing the same obfuscated gradient, or noisy gradient problem indicated by our experimental results, as the spatial transformations significantly increase the difficulty of PGD attacks. Specifically, as shown in Table 5 and Table 6, an increase in the total number of steps, whether it's the number of EoT iterations or the total iteration steps of the optimizer, consistently improves the PGD performance under spatial transformations. Additionally, we use 2048 steps in the main experiment based on these results.

**Table 5: Comparison with PGD in the patch attack on Yolo-v5s, evaluated with COCO dataset.**

Method	EoT steps	Optim. steps	$AP_{50}\downarrow$	$AP_{01}\downarrow$	time $\downarrow$
Clean	–	–	79.0%	87.6%	–
PGD	1	128	50.4%	65.7%	18.6s
	4	128	38.1%	55.2%	73.8s
	1	512	38.0%	54.5%	74.1s
	16	128	29.0%	45.2%	230.3s
	4	512	27.5%	43.3%	295.2s
	1	2048	27.0%	42.3%	296.5s
DynamicPAE	–	–	16.3%	28.8%	0.1s

**Table 6: Comparison with PGD in the patch attack on Yolo-v8n, evaluated with COCO dataset.**

Method	EoT steps	Optim. steps	$AP_{50}\downarrow$	$AP_{01}\downarrow$	time $\downarrow$
Clean	–	–	86.4%	92.1%	–
PGD	1	128	73.8%	83.5%	11.4s
	4	128	65.9%	77.6%	44.9s
	1	512	65.1%	77.1%	45.5s
	16	128	60.2%	73.9%	140.1s
	4	512	58.4%	71.7%	180.0s
	1	2048	57.7%	71.5%	181.5s
DynamicPAE	–	–	27.9%	37.8%	0.1s

The noisy gradient problem also brings severe challenges for training the dynamic generator, and our methodology focused on it. We present the performance of DynamicPAE framework after solving the problem. To ensure a fair comparison, both our model and PGD are evaluated by resampling the patch locations. Note that even with this high step count, the performance of PGD is still less aggressive than our result. In the main performance evaluation, we found that the Zero transformation settings facilitate the PGD method in achieving better results. We further analyze it on the Inria dataset. As shown in Table 7, PGD surpasses our method in attack capability at 32 steps, but our method still retains an advantage in inference time. From another perspective, the superiority of our method mainly lies in overcoming physical-world transformations.

**Table 7: Comparison with PGD in the patch attack on Yolo-v5s, evaluated with zero transformation.**

Method	EoT steps	Optim. steps	$AP_{50}\downarrow$	$AP_{01}\downarrow$	time $\downarrow$
Clean	–	–	79.0%	87.6%	–
PGD	1	8	48.0%	53.9%	1.20s
	1	32	11.5%	24.6%	4.55s
	1	128	3.4%	15.2%	17.97s
	1	512	1.7%	11.0%	71.50s
DynamicPAE	–	–	13.7%	24.8%	0.09s

**PAE Sample Space Perspective:** When training PAE generators, we find that the main challenge caused by the noisy gradient is the degenerated solution presented as mode collapse, and the theoretical modeling is constructed in section 3.1. We visualized the training result of the generated PAEs on the setting of *Yolov5, base* transformation, and COCO dataset. The results of training without the auxiliary residual task are shown in Figure 6a. Although these samples achieve attack capabilities, they exhibit significant mode collapse with only pixel-level weak differences between different samples. Figure 6b illustrates the results under the same configuration after introducing the residual task. The first row, the second row, and the last two rows represent the case with attack weight  $\lambda = 0$ ,  $\lambda = 1$ , and  $\lambda$  sampled between  $[0, 1]$ , respectively. It can be observed that the diversity of the generations is significantly enhanced.

By connecting with the proposed model, the experiment shows that: ① the formulated *limited feedback information restriction*, which models the noisy gradients and predicts the degeneracy problem of the conditional PAEs, matches the experiment results. ② By breaking the restriction of the *limited feedback information restriction*, the residual-task guided training overcomes the degeneration problem, which simultaneously demonstrates the effectiveness of the noise gradient model and method.

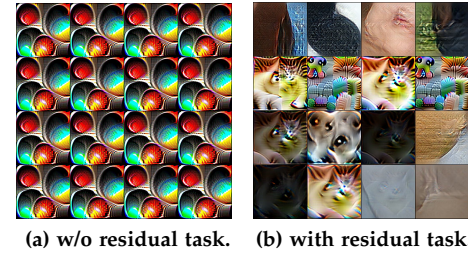


**Figure 6: Comparison of patch generation.**

In addition, this mode collapse is different from the posterior collapse in variational autoencoders (VAE), in which the noise is injected in latent  $\mathbf{Z}$  for prior-based regularization instead of stemming from the task. Moreover, although diversity is not the first goal of the attack tasks, this mode collapse is weakening the attack performance to be close to static PAEs, thus we recognize it as the degeneration problem. The comparison of the attack performance is shown in ablation studies.

### 4.3.2 Analysis and Solving the Latent Evasion Problem

**Gradient Explosion Perspective:** Another difference from training generative model on benign data is that the learning

of conditional PAE autoencoder leads to infinite gradient, and we recognize it as *latent evasion*. Experiments are conducted on identical model structures with different tasks, and the  $l_\infty$ -norm of parameter gradients are measured. The result is shown in Figure 7. Denoted as *Joint*, the maximum gradient begins to grow uncapped after 30K steps until numeric overflow. However, denoted as *Clean* and *Attack*, the  $l_\infty$ -norm curves of gradients remain normal when only fitting the PAEs and the clean sample. Thus the infinite gradient is a result specific to fitting diverse PAEs and clean data. We further analyze the maximum gradient and found that the gradient is located at the patch decoding network  $Dec : \mathcal{Z} \rightarrow \mathbb{D}$ . We argue that even though the image is generated by constraining the output to the interval  $[0, 1]$ , the hidden layer features remain unconstrained during modeling diverse PAEs, leading to the emergence of the *latent evasion*. Related theoretical analysis also shows the possibility of the infinite gradient when minimizing the VAE energy function [62]. We heuristically regularize the latent representation  $z_{adv}$ . As shown in the curve *Regularized Joint* in Figure 7, it solves the problem of infinite gradient.

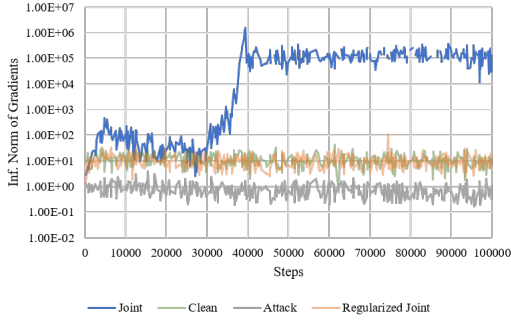


Figure 7: Inf. norm of parameter gradients in different tasks. In the case of *Joint* the gradient exploded while the regularization solves the problem.

**Latent Space Perspective:** We provide further visualized analysis on the latent space to illustrate the *latent evasion* problem and the regularization in the *supplementary material*. To interpret the learned correlation, we perform analysis based on the latent representation  $\mathbf{Z} = \text{Enc}(\mathbf{P}_X)$ . The visualized results are shown in the *supplementary material*, indicating that the model successfully learns the representation of PAEs and their correlation with the observed scenes.

#### 4.4 On the Practicality in Agnostic Attack Scenarios

To evaluate the real-world practicality of DynamicPAE when facing agnostic scenarios, we conduct experiments on different environments and parameters to show the effectiveness of the proposed simulation model. The experiments demonstrate the ability of DynamicPAE to (1) reveal potential security issues and (2) generate adversarial evaluation data that is aligned with the real world in applications.

**Results in Physical Environments:** We implement our model and deploy it with edge-computing devices (2080Ti) and the local area network (LAN), and evaluate the attack performance of the framework within the physical environment. As shown in Figure 8, our method generally achieved higher attack performance. Although our attacks

are experimental, real attacks can be realized with dynamic materials (e.g., color-changing costumes [63]) and spread through transformation simulation. Furthermore, we find that presenting the static patch in varying conditions could also the attack effectiveness, indicating that the adversarial examples generated by our method achieve a balance between attack adaptability and robustness, and the visualization, including more cases showing the adaptability and the robustness, is provided in the *supplementary material*.

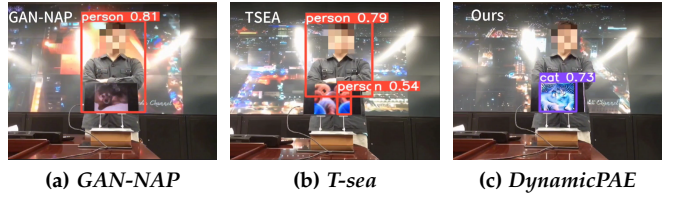


Figure 8: Our method achieves better attack performance in the scenario of the ever-changing background.

**Confirmation of Physical Robustness:** Since accurate location as model input may be difficult to obtain in applications, we perform tests with inaccurate inputs. As shown in Table 8, the attack performance did not drop much as we resample the patch locations, which is attributed to the implicit regularization of DNN and augmentation pipeline. Moreover, the attack performance is still significantly higher than the baselines in the main performance evaluation. This indicates that the model can leverage precise location information when available, while still maintaining relatively high performance even with inaccurate location inputs.

Table 8: Evaluation of the robustness against imprecise location inputs targeting Yolo-v5s on the COCO dataset. Randomized refers to re-sampling the attack locations.

Transformation	Accurate Input		Randomized	
	$AP_{50} \downarrow$	$AP_{01} \downarrow$	$AP_{50} \downarrow$	$AP_{01} \downarrow$
Base	14.9%	26.9%	16.3%	28.8%
P+	28.5%	44.7%	30.5%	46.3%
S+	17.2%	31.8%	20.7%	36.4%
AF	19.9%	36.4%	24.0%	41.0%

**Results in Simulated Environment:** To evaluate the applicability of the proposed model in the simulated testing, we obtain the simulation results from different perspectives in the CARLA autonomous driving simulation platform [64], divide them into training and testing datasets, and apply the adversarial example as a perturbation of the vehicle’s texture. Supplement to the digital environment benchmark, we compare the performance with the GAN-based perturbation generation framework *AdvGAN*, since both our model and *AdvGAN* are learning-based and real-time.

As shown in Table 9, our model also achieves strong perturbation attack performance and significantly enhances the attack aggressiveness compared to *AdvGAN*. To measure the stealthiness of the attack more accurately, we measure the SSIM similarity in addition to the  $l_\infty$  constraint. It can be seen that the attack performance of our method significantly outperforms the baseline method for all different magnitude settings. Interestingly, our method performs better in the

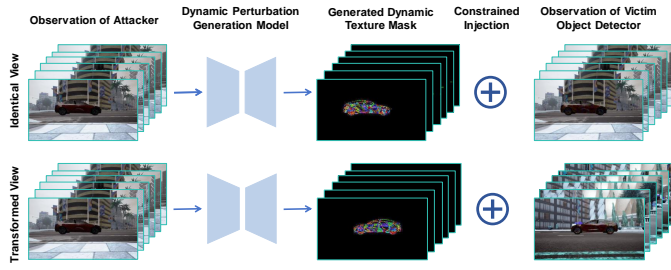


Figure 9: Demo of end-to-end simulated adversarial evaluation of autonomous driving perception systems.

transformed view than in the identical view when  $\varepsilon = 1\%$ , which may be attributed to the increased generalization due to the increased task complexity, suggesting that our method is more suitable for complex physical world attacks.

Table 9: Evaluation results on CARLA simulation. The illustration of different view settings is shown in Figure 9.

$\varepsilon$	Method	Identical View			Transformed View		
		$AP_{50}\downarrow$	$AP_{01}\downarrow$	$SSIM\uparrow$	$AP_{50}\downarrow$	$AP_{01}\downarrow$	$SSIM\uparrow$
0%	Clean	43.23%	46.56%	1.0000	51.08%	52.56%	1.0000
1%	AdvGAN	29.67%	38.40%	0.9983	34.30%	44.17%	<b>0.9994</b>
	DynamicPAE	<b>5.35%</b>	<b>12.39%</b>	<b>0.9989</b>	<b>3.31%</b>	<b>7.53%</b>	<b>0.9994</b>
5%	AdvGAN	6.0e-5	7.0e-3	0.9888	2.9e-3	1.1e-2	0.9928
	DynamicPAE	<1e-6	2.5e-6	<b>0.9969</b>	<1e-6	<b>8.5e-6</b>	<b>0.9931</b>

**Hyper-parameter Sensitivity:** Many generative models are sensitive to hyperparameters, especially GAN models, which harms their practicality. To make it clear, we present an investigation of the hyperparameters in our proposed model. The analysis includes the parameter  $\alpha_0$  as the initial weight of invisibility and  $\gamma$  in the regularization loss in Eq. 11. The results are shown in Table 10. For regularization loss, we evaluate its weight with settings  $\gamma \in \{10^{-4}, 10^{-2}, 1.0\}$ , and the attack performance remains steady, indicating that it does not require excessive parameter tuning. For the task scheduler, we evaluate it with different initial weights of invisibility  $\alpha_0$ , representing the variability in loss intensity between attack tasks, and both the auto-adjusted weight  $\alpha_{final}$  and evaluation results remain similar, indicating the functionality of the skewness-based objective re-weighting mechanism that eliminates the free parameter and strike a consistent balance between attack and stealthiness. Moreover, on the aggressiveness-distortion curves of the main performance experiments, the uniform and consistent data point distribution of our method across the different models also indicates it.

#### 4.5 Ablation Studies

**Auxiliary Residual Task:** Ablation experiments across different target models and different patch transformations are conducted to evaluate the residual task.  $\lambda$  is set to 1 during tests. As shown in Figure 11, the constructed auxiliary residual task consistently improves the attack performance of dynamic PAE, demonstrating the necessity of such construction in the dynamic PAE optimization process. We recognize that the improvement is more significant in large victim models that are hard to attack, including *Yolo-v5m* and *Faster-RCNN*, which may be because larger models

Table 10: Analysis of parameter sensitivity. The weight of regularization  $\gamma$  is insensitive and the sensitivity of the weight of the residual task is reduced by the *skewness-aligned objective re-weighting* method.

$\gamma$	$\alpha_0$	$\alpha_{final}$	$\lambda = 1.0$		$\lambda = 0.5$	
			$AP_{50}\downarrow$	$SSIM\uparrow$	$AP_{50}\downarrow$	$SSIM\uparrow$
1.0	100.0	33.05	14.31%	0.9891	38.48%	0.9929
0.01	100.0	33.42	14.07%	0.9891	35.63%	0.9928
1e-4	100.0	30.31	14.02%	0.9890	34.29%	0.9928
1.0	1.0	35.77	14.90%	0.9891	31.99%	0.9927
1.0	10.0	36.85	15.50%	0.9892	32.86%	0.9925

have more diverse vulnerabilities, allowing for the discovery of more conditional solutions through the improved optimization process. We also recognize that in the setting of  $P+$ , where the spatial transformation in attack injection  $\oplus$  is more diverse, the drop ratio of  $AP$  is relatively low. This may be because of higher uncertainty makes the information available for adaptation limited, with less room for performance improvement. It is worth exploring how to construct more effective residual tasks or alter attack tasks to further enhance attack capabilities.

Table 11: Ablation study of the auxiliary residual task. By collaborating with the attack training, the residual task consistently improves the attack performance compared to vanilla training (in columns w/o).

Model	Configs	+ Residual Task		w/o	
		Trans.	$AP_{50}\downarrow$	$AP_{01}\downarrow$	$AP_{50}\downarrow$
Yolov5-s	Base	14.87%	26.94%	29.34%	48.59%
Yolov5-m	Base	26.43%	36.00%	42.02%	55.89%
Yolov3-m	Base	6.24%	10.18%	8.23%	11.57%
FSCNN	Base	26.33%	27.89%	65.63%	67.93%
Yolov8-n	Base	26.04%	35.85%	40.82%	46.12%
Yolov5-s	P+	28.46%	44.68%	32.96%	49.40%
Yolov5-s	Zero	9.70%	23.68%	16.04%	21.64%
Yolov5-s	S+	17.15%	31.76%	22.39%	39.34%
Yolov5-s	AF	19.87%	36.44%	31.73%	49.51%

**Latent Regularization:** We compare the differences among regularization in terms of the attack performance. As shown in Table 12, the center-regularized  $z_{adv}$  achieves the optimal performance among different settings and solves the problem of gradient explosion when learning diverse PAEs through the auxiliary residual task. Note that without the auxiliary residual task (Aux. Task), the PAE decoder Dec degenerates to a single static PAE. We noticed classical VAE regularization still suffers the infinite gradient in the model of Yolo-v8n and the attack performance on Yolo-v5 is lower, indicating the widely-used Gaussian prior might not be a proper selection for the latent of explored PAEs.

## 5 RELATED WORKS

**Digital Adversarial Example Generation:** Classical type of AE research concentrated on generating  $l_p$ -constrained examples and developed techniques based on model gradient [28], projected gradient descent [59], SGD optimizer [65] and neural network [66]. Further study focused on constructing more complex attack scenarios, such as the black-box attack [67], data-manifold constrained AEs [68], and the transfer attacks among models and scenarios.

**Table 12: Ablation of latent regularization. Encouraging the codewords of PAEs to be located in the center of the representation space achieves better attack performance and training stability.**

$z_{adv}$	Aux. Task	Model	$AP_{50} \downarrow$	$AP_{01} \downarrow$
w/o regularization	✗	v5	22.39%	40.66%
	✗	v8	39.96%	45.33%
	✓	v5/8	— (Gradient Exploded)	
$\sim \mathcal{N}(0, I)$ (VAE prior)	✗	v5	18.97%	35.16%
	✗	v8	44.95%	50.53%
	✓	v5	17.66%	34.00%
	✓	v8	— (Gradient Exploded)	
$l_2$ -norm ( <i>DynamicPAE</i> Applied)	✗	v5	29.34%	48.59%
	✗	v8	40.82%	46.12%
	✓	v5	14.87%	26.72%
	✓	v8	26.04%	35.85%

**Physical Adversarial Attacks:** Based on the paradigm of optimizing static PAEs, research focuses on simulating the physical world [69] and the target AI system [20], and modeling PAEs under naturalness constrains [42] or new attack mediums [70]. Recent works began to focus on the challenge of generating dynamic PAEs. [24] proposes the *Dynamic Adversarial Patch* on the dynamically changing clothes, while the PAE data itself is still static. [23] proposes the adaptive PAE by manually clustering the attack scenario and optimizing the static PAE for each cluster, but it is not suitable for the open world. [22] proposes a physical adversarial attack by controlling a dynamic laser beam in the simulation using reinforcement learning. Nevertheless, it is only capable of modeling a limited number of laser states but not the general space of PAE.

**Generative Models and Generative Adversarial Attacks:** Motivated by learning representations [71], classical generative neural networks adapt generative learning methods to train a model that maps the space of real data  $\mathcal{X}$  to a latent space  $\mathcal{Z}$ , which has better mapping modeling and sampling efficiency. With refined learning tasks and neural network construction [49], [72], generative models is able to generate complex data, *e.g.*, model the relation of texts and natural images [73], molecular dynamics [74], protein structure [75] and images and corresponding digital perturbation AEs [37]. In terms of adversarial attacks, NN-based generators have been applied in improving perturbation optimization [37], generating naturalistic AEs by modeling the data manifold [21], [42], [68], [76] and probabilistic modeling perturbations for black-box attacks [77]. However, only *unconditional & static* PAEs have been proposed under the generative framework [42], [76], [78]. Except for some specific adversarial attack mediums, *e.g.*, audio [79] and face subspace [70], the physical-digital gap [18] is small, the randomized transformation may not be necessary, and therefore the digital AE generation network may be effective. As an important step forward, we bridge the general gap between scene-aware dynamic PAE and generative NNs.

**Multidisciplinary Optimization Techniques:** Similar optimization problems also occurred in the application of neural networks [80] that learns complex tasks in the field of AI4Science, *e.g.*, approximating complex fields [81] and training on noisy measurements [82]. We believe the

relevant research will be beneficial for scene-aware PAE generation, and visa versa. In the field of reinforcement learning, research has been conducted on the problem of exploring the action space and utilizing inaccurate feedback [83]. However, the general scene-aware PAE generation problem is defined in the complex state space, such as a patch with 10K+ pixels, which cannot be intractable for reinforcement models. Recently, language-driven models have been adapted for optimization [84], but there is still a gap between language and low-level AE data [85], which should be filled by the generative embedding model.

## 6 CONCLUSIONS

This study focuses on the dynamic physical adversarial examples (PAEs), a fundamental and largely unaddressed vulnerability of deep learning models in applications. A highly effective and versatile method, DynamicPAE, is proposed for generating real-time scene-aware PAE, offering a significant advancement. Extensive experimental results demonstrate that the proposed method exhibits superior dynamic attack performance in open and complex scenarios.

Future research directions can focus on technical improvements to the patch representation and training mechanism, exploring the application of the proposed framework, and facilitating the developed techniques in broader domains. In terms of application, although we have presented the preliminary prototype in our experiments, work on generating adversarial test and training data and exploring real-world red team attacks for specific tasks is still worthy of further investigation. We believe that our study has the broader potential to benefit the optimization of defense-insensitive adversarial attacks and noisy open-world tasks, and the model for the hardness of PAE optimization can bring insights to the defense of PAEs. In addition, the proposed scene-aware PAE generation task is representative and beneficial for foundation model research.

## ACKNOWLEDGMENTS

This work is supported by Zhongguancun Laboratory and State Key Laboratory of Complex & Critical Software Environment (CCSE).

## REFERENCES

- [1] L. Chen, P. Wu, K. Chitta, B. Jaeger, A. Geiger, and H. Li, “End-to-end autonomous driving: Challenges and frontiers,” *IEEE Transactions on Pattern Analysis and Machine Intelligence*, pp. 1–20, 2024.
- [2] A. Esteva, A. Robicquet, B. Ramsundar, V. Kuleshov, M. DePristo, K. Chou, C. Cui, G. Corrado, S. Thrun, and J. Dean, “A guide to deep learning in healthcare,” *Nature medicine*, vol. 25, no. 1, pp. 24–29, 2019.
- [3] W. X. Zhao, K. Zhou, J. Li, T. Tang, X. Wang, Y. Hou, Y. Min, B. Zhang, J. Zhang, Z. Dong *et al.*, “A survey of large language models,” *arXiv preprint arXiv:2303.18223*, 2023.
- [4] C. Szegedy, W. Zaremba, I. Sutskever, J. Bruna, D. Erhan, I. Goodfellow, and R. Fergus, “Intriguing properties of neural networks,” *arXiv preprint arXiv:1312.6199*, 2013.
- [5] J. Peck, B. Goossens, and Y. Saeys, “An introduction to adversarially robust deep learning,” *IEEE Transactions on Pattern Analysis and Machine Intelligence*, vol. 46, no. 4, pp. 2071–2090, 2024.
- [6] J. Wang, A. Liu, X. Bai, and X. Liu, “Universal adversarial patch attack for automatic checkout using perceptual and attentional bias,” *IEEE Transactions on Image Processing*, vol. 31, pp. 598–611, 2021.

[7] J. Wang, A. Liu, Z. Yin, S. Liu, S. Tang, and X. Liu, "Dual attention suppression attack: Generate adversarial camouflage in physical world," in *Proceedings of the IEEE/CVF Conference on Computer Vision and Pattern Recognition*, 2021, pp. 8565–8574.

[8] N. Wang, Y. Luo, T. Sato, K. Xu, and Q. A. Chen, "Does physical adversarial example really matter to autonomous driving? towards system-level effect of adversarial object evasion attack," in *Proceedings of the IEEE/CVF International Conference on Computer Vision (ICCV)*, October 2023, pp. 4412–4423.

[9] A. Liu, J. Guo, J. Wang, S. Liang, R. Tao, W. Zhou, C. Liu, X. Liu, and D. Tao, "{X-Adv}: Physical adversarial object attacks against x-ray prohibited item detection," in *32nd USENIX Security Symposium (USENIX Security 23)*, 2023, pp. 3781–3798.

[10] W. Ding, C. Xu, M. Arief, H. Lin, B. Li, and D. Zhao, "A survey on safety-critical scenario generation for autonomous driving—a methodological perspective," *arXiv preprint arXiv:2202.02215*, 2022.

[11] H. Zhang, S. Jiang, X. Wang, W. Zhang, X. Huang, X. Ouyang, Y. Yu, Y. Liu, D.-L. Deng, and L.-M. Duan, "Experimental demonstration of adversarial examples in learning topological phases," *Nature communications*, vol. 13, no. 1, p. 4993, 2022.

[12] A. Ilyas, S. Santurkar, D. Tsipras, L. Engstrom, B. Tran, and A. Madry, "Adversarial examples are not bugs, they are features," *Advances in neural information processing systems*, vol. 32, 2019.

[13] D. Yin, R. Kannan, and P. Bartlett, "Rademacher complexity for adversarially robust generalization," in *International conference on machine learning*. PMLR, 2019, pp. 7085–7094.

[14] Y.-S. Lin, W.-C. Lee, and Z. B. Celik, "What do you see? evaluation of explainable artificial intelligence (xai) interpretability through neural backdoors," in *Proceedings of the 27th ACM SIGKDD conference on knowledge discovery & data mining*, 2021, pp. 1027–1035.

[15] J. Guo, A. Li, and C. Liu, "AEVA: Black-box backdoor detection using adversarial extreme value analysis," in *International Conference on Learning Representations*, 2022.

[16] J. Wang, X. Liu, J. Hu, D. Wang, S. Wu, T. Jiang, Y. Guo, A. Liu, and J. Zhou, "Adversarial examples in the physical world: A survey," *arXiv preprint arXiv:2311.01473*, 2024.

[17] D. Song, K. Eykholt, I. Evtimov, E. Fernandes, B. Li, A. Rahmati, F. Tramèr, A. Prakash, and T. Kohno, "Physical adversarial examples for object detectors," in *12th USENIX Workshop on Offensive Technologies (WOOT 18)*. Baltimore, MD: USENIX Association, Aug. 2018.

[18] A. Kurakin, I. J. Goodfellow, and S. Bengio, "Adversarial examples in the physical world," in *5th International Conference on Learning Representations, ICLR 2017, Toulon, France, April 24-26, 2017, Workshop Track Proceedings*. OpenReview.net, 2017.

[19] K. Eykholt, I. Evtimov, E. Fernandes, B. Li, A. Rahmati, C. Xiao, A. Prakash, T. Kohno, and D. Song, "Robust physical-world attacks on deep learning visual classification," in *Proceedings of the IEEE conference on computer vision and pattern recognition*, 2018, pp. 1625–1634.

[20] Z. Zhu, Y. Zhang, H. Chen, Y. Dong, S. Zhao, W. Ding, J. Zhong, and S. Zheng, "Understanding the robustness of 3d object detection with bird's-eye-view representations in autonomous driving," in *Proceedings of the IEEE/CVF Conference on Computer Vision and Pattern Recognition*, 2023, pp. 21600–21610.

[21] A. Liu, X. Liu, J. Fan, Y. Ma, A. Zhang, H. Xie, and D. Tao, "Perceptual-sensitive gan for generating adversarial patches," in *Proceedings of the AAAI conference on artificial intelligence*, vol. 33, no. 01, 2019, pp. 1028–1035.

[22] Y. Sun, Y. Huang, and X. Wei, "Embodied laser attack:leveraging scene priors to achieve agent-based robust non-contact attacks," in *ACM Multimedia 2024*, 2024.

[23] A. Chahe, C. Wang, A. Jeyaprakash, K. Xu, and L. Zhou, "Dynamic adversarial attacks on autonomous driving systems," *arXiv preprint arXiv:2312.06701*, 2023.

[24] A. Guesmi, R. Ding, M. A. Hanif, I. Alouani, and M. Shafique, "Dap: A dynamic adversarial patch for evading person detectors," in *Proceedings of the IEEE/CVF Conference on Computer Vision and Pattern Recognition*, 2024, pp. 24595–24604.

[25] A. Athalye, N. Carlini, and D. Wagner, "Obfuscated gradients give a false sense of security: Circumventing defenses to adversarial examples," in *International conference on machine learning*. PMLR, 2018, pp. 274–283.

[26] X. Ma, B. Li, Y. Wang, S. M. Erfani, S. N. R. Wijewickrema, G. Schoenebeck, D. Song, M. E. Houle, and J. Bailey, "Characterizing adversarial subspaces using local intrinsic dimensionality," in *6th International Conference on Learning Representations, ICLR 2018, Vancouver, BC, Canada, April 30 - May 3, 2018, Conference Track Proceedings*. OpenReview.net, 2018.

[27] K. He, X. Zhang, S. Ren, and J. Sun, "Deep residual learning for image recognition," in *Proceedings of the IEEE conference on computer vision and pattern recognition*, 2016, pp. 770–778.

[28] I. J. Goodfellow, J. Shlens, and C. Szegedy, "Explaining and harnessing adversarial examples," in *3rd International Conference on Learning Representations, ICLR 2015, San Diego, CA, USA, May 7-9, 2015, Conference Track Proceedings*, 2015.

[29] A. Athalye, L. Engstrom, A. Ilyas, and K. Kwok, "Synthesizing Robust Adversarial Examples," *arXiv e-prints*, p. arXiv:1707.07397, Jul. 2017.

[30] S. Wolfram, "Origins of randomness in physical systems," *Physical Review Letters*, vol. 55, no. 5, p. 449, 1985.

[31] Q. Dai, J. Zhang, Q. Li, T. Wu, H. Dong, Z. Liu, P. Tan, and H. Wang, "Domain randomization-enhanced depth simulation and restoration for perceiving and grasping specular and transparent objects," in *European Conference on Computer Vision*. Springer, 2022, pp. 374–391.

[32] F. Muratore, M. Gienger, and J. Peters, "Assessing transferability from simulation to reality for reinforcement learning," *IEEE Transactions on Pattern Analysis and Machine Intelligence*, vol. 43, no. 4, pp. 1172–1183, 2021.

[33] H. Wei, H. Tang, X. Jia, Z. Wang, H. Yu, Z. Li, S. Satoh, L. Van Gool, and Z. Wang, "Physical adversarial attack meets computer vision: A decade survey," *IEEE Transactions on Pattern Analysis and Machine Intelligence*, pp. 1–20, 2024.

[34] Y. Zhao, H. Zhu, R. Liang, Q. Shen, S. Zhang, and K. Chen, "Seeing isn't believing: Towards more robust adversarial attack against real world object detectors," in *Proceedings of the 2019 ACM SIGSAC conference on computer and communications security*, 2019, pp. 1989–2004.

[35] Y. Huang, Y. Dong, S. Ruan, X. Yang, H. Su, and X. Wei, "Towards transferable targeted 3d adversarial attack in the physical world," in *Proceedings of the IEEE/CVF Conference on Computer Vision and Pattern Recognition*, 2024, pp. 24512–24522.

[36] X. Wei, Y. Huang, Y. Sun, and J. Yu, "Unified adversarial patch for visible-infrared cross-modal attacks in the physical world," *IEEE Transactions on Pattern Analysis and Machine Intelligence*, vol. 46, no. 4, pp. 2348–2363, 2024.

[37] C. Xiao, B. Li, J.-Y. Zhu, W. He, M. Liu, and D. Song, "Generating adversarial examples with adversarial networks," *arXiv preprint arXiv:1801.02610*, 2018.

[38] X. Wei, Y. Guo, J. Yu, and B. Zhang, "Simultaneously optimizing perturbations and positions for black-box adversarial patch attacks," *IEEE Transactions on Pattern Analysis and Machine Intelligence*, vol. 45, no. 7, pp. 9041–9054, 2022.

[39] T. B. Brown, D. Mané, A. Roy, M. Abadi, and J. Gilmer, "Adversarial Patch," *arXiv e-prints*, p. arXiv:1712.09665, Dec. 2017.

[40] S. Liu, J. Wang, A. Liu, Y. Li, Y. Gao, X. Liu, and D. Tao, "Harnessing perceptual adversarial patches for crowd counting," in *Proceedings of the 2022 ACM SIGSAC Conference on Computer and Communications Security*, ser. CCS '22. New York, NY, USA: Association for Computing Machinery, 2022, p. 2055–2069.

[41] S. Zhang, Y. Cheng, W. Zhu, X. Ji, and W. Xu, "CAPatch: Physical adversarial patch against image captioning systems," in *32nd USENIX Security Symposium (USENIX Security 23)*. Anaheim, CA: USENIX Association, Aug. 2023, pp. 679–696.

[42] Y. Hu, J.-C. Chen, B.-H. Kung, K.-L. Hua, and D. S. Tan, "Naturalistic physical adversarial patch for object detectors," *2021 IEEE/CVF International Conference on Computer Vision (ICCV)*, pp. 7828–7837, 2021.

[43] H. Huang, Z. Chen, H. Chen, Y. Wang, and K. Zhang, "T-sea: Transfer-based self-ensemble attack on object detection," in *2023 IEEE/CVF Conference on Computer Vision and Pattern Recognition (CVPR)*. Los Alamitos, CA, USA: IEEE Computer Society, jun 2023, pp. 20514–20523.

[44] M. Kang, D. Song, and B. Li, "Diffattack: Evasion attacks against diffusion-based adversarial purification," *Advances in Neural Information Processing Systems*, vol. 36, 2024.

[45] S.-M. Moosavi-Dezfooli, A. Fawzi, O. Fawzi, and P. Frossard, "Universal adversarial perturbations," in *Proceedings of the IEEE conference on computer vision and pattern recognition*, 2017, pp. 1765–1773.

[46] U. Tanielian, T. Issenhuth, E. Dohmatob, and J. Mary, "Learning disconnected manifolds: a no GAN's land," in *Proceedings of the*

37th International Conference on Machine Learning, ser. Proceedings of Machine Learning Research, vol. 119. PMLR, 13–18 Jul 2020, pp. 9418–9427.

[47] S. Durr, Y. Mroueh, Y. Tu, and S. Wang, “Effective dynamics of generative adversarial networks,” *Physical Review X*, vol. 13, no. 4, p. 041004, 2023.

[48] J.-Y. Franceschi, M. Gartrell, L. Dos Santos, T. Issenhuth, E. de Bézenac, M. Chen, and A. Rakotomamonjy, “Unifying gans and score-based diffusion as generative particle models,” *Advances in Neural Information Processing Systems*, vol. 36, 2024.

[49] Y. Song and S. Ermon, “Generative modeling by estimating gradients of the data distribution,” in *Advances in Neural Information Processing Systems*, vol. 32. Curran Associates, Inc., 2019.

[50] R. Zhang, P. Isola, A. A. Efros, E. Shechtman, and O. Wang, “The unreasonable effectiveness of deep features as a perceptual metric,” in *Proceedings of the IEEE conference on computer vision and pattern recognition*, 2018, pp. 586–595.

[51] J. Yu and T. S. Huang, “Universally slimmable networks and improved training techniques,” in *Proceedings of the IEEE/CVF international conference on computer vision*, 2019, pp. 1803–1811.

[52] L. I. Rudin, S. Osher, and E. Fatemi, “Nonlinear total variation based noise removal algorithms,” *Physica D: nonlinear phenomena*, vol. 60, no. 1-4, pp. 259–268, 1992.

[53] J. Wang, X. Liu, Z. Yin, Y. Wang, J. Guo, H. Qin, Q. Wu, and A. Liu, “Generate transferable adversarial physical camouflages via triplet attention suppression,” *International Journal of Computer Vision*, pp. 1–17, 2024.

[54] E. D. Cubuk, B. Zoph, J. Shlens, and Q. Le, “RandAugment: Practical automated data augmentation with a reduced search space,” in *Advances in Neural Information Processing Systems*, vol. 33. Curran Associates, Inc., 2020, pp. 18613–18624.

[55] R. A. Groeneveld and G. Meeden, “Measuring skewness and kurtosis,” *Journal of the Royal Statistical Society Series D: The Statistician*, vol. 33, no. 4, pp. 391–399, 1984.

[56] I. Higgins, L. Matthey, A. Pal, C. Burgess, X. Glorot, M. Botvinick, S. Mohamed, and A. Lerchner, “beta-vae: Learning basic visual concepts with a constrained variational framework,” in *International conference on learning representations*, 2016.

[57] T.-Y. Lin, M. Maire, S. Belongie, L. Bourdev, R. Girshick, J. Hays, P. Perona, D. Ramanan, C. L. Zitnick, and P. Dollár, “Microsoft coco: Common objects in context,” 2015.

[58] N. Dalal and B. Triggs, “Histograms of oriented gradients for human detection,” in *2005 IEEE computer society conference on computer vision and pattern recognition (CVPR’05)*, vol. 1. Ieee, 2005, pp. 886–893.

[59] A. Madry, A. Makelov, L. Schmidt, D. Tsipras, and A. Vladu, “Towards deep learning models resistant to adversarial attacks,” *arXiv preprint arXiv:1706.06083*, 2017.

[60] Y. Song, T. Kim, S. Nowozin, S. Ermon, and N. Kushman, “Pixeldefend: Leveraging generative models to understand and defend against adversarial examples,” *ArXiv*, vol. abs/1710.10766, 2017.

[61] S. Wu, J. Wang, J. Zhao, Y. Wang, and X. Liu, “Napguard: Towards detecting naturalistic adversarial patches,” in *Proceedings of the IEEE/CVF Conference on Computer Vision and Pattern Recognition*, 2024, pp. 24367–24376.

[62] B. Dai, L. Wenliang, and D. Wipf, “On the value of infinite gradients in variational autoencoder models,” *Advances in Neural Information Processing Systems*, vol. 34, pp. 7180–7192, 2021.

[63] H. Kim, J. Choi, K. K. Kim, P. Won, S. Hong, and S. H. Ko, “Biomimetic chameleon soft robot with artificial crypsis and disruptive coloration skin,” *Nature communications*, vol. 12, no. 1, p. 4658, 2021.

[64] A. Dosovitskiy, G. Ros, F. Codevilla, A. Lopez, and V. Koltun, “CARLA: An open urban driving simulator,” in *Proceedings of the 1st Annual Conference on Robot Learning*, ser. Proceedings of Machine Learning Research, S. Levine, V. Vanhoucke, and K. Goldberg, Eds., vol. 78. PMLR, 13–15 Nov 2017, pp. 1–16.

[65] N. Carlini and D. A. Wagner, “Towards evaluating the robustness of neural networks,” in *2017 IEEE Symposium on Security and Privacy, SP 2017, San Jose, CA, USA, May 22–26, 2017*. IEEE Computer Society, 2017, pp. 39–57.

[66] S. Baluja and I. Fischer, “Adversarial transformation networks: Learning to generate adversarial examples,” *arXiv preprint arXiv:1703.09387*, 2017.

[67] P.-Y. Chen, H. Zhang, Y. Sharma, J. Yi, and C.-J. Hsieh, “Zoo: Zeroth order optimization based black-box attacks to deep neural networks without training substitute models,” in *Proceedings of the 10th ACM workshop on artificial intelligence and security*, 2017, pp. 15–26.

[68] Y. Song, R. Shu, N. Kushman, and S. Ermon, “Constructing unrestricted adversarial examples with generative models,” in *Advances in Neural Information Processing Systems 31: Annual Conference on Neural Information Processing Systems 2018, NeurIPS 2018, December 3–8, 2018, Montréal, Canada*, 2018, pp. 8322–8333.

[69] S. T. Jan, J. Messou, Y.-C. Lin, J.-B. Huang, and G. Wang, “Connecting the digital and physical world: Improving the robustness of adversarial attacks,” in *Proceedings of the AAAI Conference on Artificial Intelligence*, vol. 33, 2019, pp. 962–969.

[70] X. Yang, C. Liu, L. Xu, Y. Wang, Y. Dong, N. Chen, H. Su, and J. Zhu, “Towards effective adversarial textured 3d meshes on physical face recognition,” in *Proceedings of the IEEE/CVF Conference on Computer Vision and Pattern Recognition*, 2023, pp. 4119–4128.

[71] Y. Bengio, A. Courville, and P. Vincent, “Representation learning: A review and new perspectives,” *IEEE Transactions on Pattern Analysis and Machine Intelligence*, vol. 35, no. 8, pp. 1798–1828, 2013.

[72] K. Tian, Y. Jiang, Z. Yuan, B. Peng, and L. Wang, “Visual autoregressive modeling: Scalable image generation via next-scale prediction,” *arXiv preprint arXiv:2404.02905*, 2024.

[73] A. Q. Nichol, P. Dhariwal, A. Ramesh, P. Shyam, P. Mishkin, B. McGrew, I. Sutskever, and M. Chen, “GLIDE: Towards photorealistic image generation and editing with text-guided diffusion models,” in *Proceedings of the 39th International Conference on Machine Learning*, ser. Proceedings of Machine Learning Research, K. Chaudhuri, S. Jegelka, L. Song, C. Szepesvari, G. Niu, and S. Sabato, Eds., vol. 162. PMLR, 17–23 Jul 2022, pp. 16784–16804.

[74] L. Zhang, J. Han, H. Wang, R. Car, and W. E, “Deep potential molecular dynamics: a scalable model with the accuracy of quantum mechanics,” *Physical review letters*, vol. 120, no. 14, p. 143001, 2018.

[75] A. Morehead and J. Cheng, “Geometry-complete diffusion for 3d molecule generation and optimization,” *Communications Chemistry*, vol. 7, no. 1, p. 150, 2024.

[76] H. Xue, A. Araujo, B. Hu, and Y. Chen, “Diffusion-based adversarial sample generation for improved stealthiness and controllability,” in *Advances in Neural Information Processing Systems*, A. Oh, T. Naumann, A. Globerson, K. Saenko, M. Hardt, and S. Levine, Eds., vol. 36. Curran Associates, Inc., 2023, pp. 2894–2921.

[77] F. Yin, Y. Zhang, B. Wu, Y. Feng, J. Zhang, Y. Fan, and Y. Yang, “Generalizable black-box adversarial attack with meta learning,” *IEEE Trans. Pattern Anal. Mach. Intell.*, vol. 46, no. 3, pp. 1804–1818, 2024.

[78] Z. Hu, S. Huang, X. Zhu, F. Sun, B. Zhang, and X. Hu, “Adversarial texture for fooling person detectors in the physical world,” in *Proceedings of the IEEE/CVF conference on computer vision and pattern recognition*, 2022, pp. 13307–13316.

[79] M. Chiquier, C. Mao, and C. Vondrick, “Real-time neural voice camouflage,” in *The Tenth International Conference on Learning Representations, ICLR 2022, Virtual Event, April 25–29, 2022*. OpenReview.net, 2022.

[80] M. Raissi, P. Perdikaris, and G. E. Karniadakis, “Physics-informed neural networks: A deep learning framework for solving forward and inverse problems involving nonlinear partial differential equations,” *Journal of Computational physics*, vol. 378, pp. 686–707, 2019.

[81] A. Krishnapriyan, A. Gholami, S. Zhe, R. Kirby, and M. W. Mahoney, “Characterizing possible failure modes in physics-informed neural networks,” *Advances in Neural Information Processing Systems*, vol. 34, pp. 26548–26560, 2021.

[82] L. Yuan, Y.-Q. Ni, X.-Y. Deng, and S. Hao, “A-pinn: Auxiliary physics informed neural networks for forward and inverse problems of nonlinear integro-differential equations,” *Journal of Computational Physics*, vol. 462, p. 111260, 2022.

[83] C. Colas, O. Sigaud, and P.-Y. Oudeyer, “GEP-PG: Decoupling exploration and exploitation in deep reinforcement learning algorithms,” in *Proceedings of the 35th International Conference on Machine Learning*, ser. Proceedings of Machine Learning Research, J. Dy and A. Krause, Eds., vol. 80. PMLR, 10–15 Jul 2018, pp. 1039–1048.

[84] C. Yang, X. Wang, Y. Lu, H. Liu, Q. V. Le, D. Zhou, and X. Chen, “Large language models as optimizers,” in *The Twelfth International Conference on Learning Representations*, 2024.

[85] N. Carlini, M. Nasr, C. A. Choquette-Choo, M. Jagielski, I. Gao, P. W. W. Koh, D. Ippolito, F. Tramer, and L. Schmidt, “Are aligned

neural networks adversarially aligned?" *Advances in Neural Information Processing Systems*, vol. 36, 2024.

[86] H. Kim, "Torchattacks: A pytorch repository for adversarial attacks," *arXiv preprint arXiv:2010.01950*, 2020.



**Jin Hu** is currently a Ph.D. Student at the State Key Laboratory of Complex & Critical Software Environment, Beihang University and Zhongguancun Lab. His research interests include adversarial machine learning, generative modeling, and trustworthy AI.



**Xianqi Yang** is now an engineer at Zhongguancun Laboratory, Beijing, China. He received the master's degree in 2023 from Beihang University, supervised by Prof. Qing Gao and Prof. Kexin Liu. His research interests are blockchain(mainly) and industrial security.



**Xianglong Liu** is a Full Professor in School of Computer Science and Engineering at Beihang University. He received BS and Ph.D degrees under supervision of Prof. Wei Li, and visited DVMM Lab, Columbia University as a joint Ph.D student supervised by Prof. Shih-Fu Chang. His research interests include fast visual computing (e.g., large-scale search/understanding) and robust deep learning (e.g., network quantization, adversarial attack/defense, few shot learning).

He received NSFC Excellent Young Scientists Fund, and was selected into 2019 Beijing Nova Program, MSRA Star-Track Program, and 2015 CCF Young Talents Development Program.



**Haotong Qin** is a Postdoctoral Researcher at the Center for Project-Based Learning (PBL), ETH Zürich, Switzerland, working with PD Dr. Michele Magno. Previously, he received my Ph.D. degree from the State Key Laboratory of Complex & Critical Software Environment (SKL-CCSE), Beihang University in 2024, supervised by Prof. Wei Li and Prof. Xianglong Liu. He was a visiting PhD student at Computer Vision Lab, ETH Zürich. He obtained B.E. degree from SCSE, Beihang University in 2019. He interned at ByteDance AI Lab, Tencent WXG, and Microsoft Research Asia. His research interest broadly includes efficient deep learning.



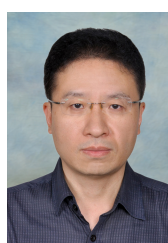
**Jiakai Wang** is now a Research Scientist in Zhongguancun Laboratory, Beijing, China. He received the Ph.D. degree in 2022 from Beihang University (Summa Cum Laude), supervised by Prof. Wei Li and Prof. Xianglong Liu. Before that, he obtained his BSc degree in 2018 from Beihang University (Summa Cum Laude). His research interests are Trustworthy AI in Computer Vision (mainly) and Multimodal Machine Learning, including Physical Adversarial Attacks and Defense and Security of Practical AI.



**Yuqing Ma** received the Ph.D degree in 2021 from Beihang University, China. She was a postdoctoral fellow at Beihang University from 2021 to 2023. She is currently an associate professor with the Institute of Artificial Intelligence at Beihang University. Her current research interests include computer vision, few-shot learning and open world learning. She has published nearly 30 research papers at top-tier conferences and journals.



**Junkai Zhang** is currently a research intern at State Key Laboratory of Complex & Critical Software Environment, Beihang University, and a BEng student at the joint cultivation program of Beihang University and Beijing University of Technology. His research interests include computational linguistics and trustworthy AI.



**Ke Xu** received the BE, ME, and PhD degrees from Beihang University, in 1993, 1996, and 2000, respectively. He is a professor at the School of Computer Science and Engineering, Beihang University, China. His current research interests include phase transitions in NP-Complete problems, algorithm design, computational complexity, big spatio-temporal data analytics, crowdsourcing, and crowd intelligence.

## SUPPLEMENTARY MATERIALS

### 1 EXPERIMENT SETTINGS

#### 1.1 Benchmark Settings

**Datasets:** We use the COCO [57] and the Inria [58] as the dataset of the person detection task, while data collected from CARLA is used for the simulation experiment. For COCO, bounding boxes marked as crowds or smaller than 1/36 of the image, resulting in about 60,000 training boxes and 2,500 testing boxes are filtered out in both training and evaluation. Inria is a smaller and cleaner dataset for pedestrian detection, containing about 1,200 training boxes and 300 testing boxes. We did not filter Inria bounding boxes. We attacked and evaluated individual objects directly from the datasets, allowing precise assessment of attack performance on different objects within a single image.

**Attack Simulation:** We mainly evaluate our model under simulated physical adversarial attack to enable more accurate numerical analysis. We define a patch placement model for evaluation based on affine transformation  $A$ , which can be decomposed into rotation matrices, scaling matrices, and translation matrices:

$$A = A_{rotate} \cdot A_{scale} \cdot A_{trans}. \quad (21)$$

Thus, we define separate parameter distribution models for rotation, scaling, and translation in the transformation. Specifically, we sample the relative position and size of the patch for the candidate bounding box, as well as the parameters for rotation in the 2D space of the image and rotation in the 3D space (the rotation axis is parallel to the camera's imaging plane), from a predefined uniform distribution shown in Table 13. In comparison to previous evaluations, a setting of smaller patch size was implemented across the evaluated attacks, which increases the attack difficulty. For color distortion, we apply brightness, saturation, and contrast transformation with uniform sampled parameters, and add Gaussian noise with standard variance sampled from the uniform distribution, as shown in Table 14. For each image and each selected bounding box in the test set, 10 random transformation parameters are sampled to expand the evaluation scale. We provide a visualized example of evaluation in Figure 10.

**Table 13: Spatial Transformation Settings**

Name	Position	Size	Rotation	3D Rotation
Zero	0.5	0.05	0	0
Base	[0.4, 0.6]	[0.04, 0.06]	[-9°, +9°]	0
S+	[0.4, 0.6]	[0.03, 0.07]	[-9°, +9°]	0
P+	[0.3, 0.7]	[0.04, 0.06]	[-9°, +9°]	0
AF	[0.4, 0.6]	[0.04, 0.06]	[-9°, +9°]	[-30°, +30°]

**Table 14: Color Transformation Settings**

	Brightness	Saturation	Contrast	Gaussian Noise
Param.	±0.05	±0.1	±0.1	[0, 0.02]



**Figure 10: Example of patch attack evaluation on COCO dataset. The spatial transformation setting is Base.**

#### 1.2 Method Implementations

**Neural Network Architecture of DynamicPAE:** To efficiently and robustly model the complex correlation, a unified representation learning paradigm with encoder-decoder architecture is applied for the PAE generator to fit the correlation in the high-level representation space, which formulates  $\mathcal{G}$  as  $\mathcal{G} := \text{Dec} \circ \text{Enc}$ ,  $\text{Enc} : \mathcal{P} \rightarrow \mathcal{Z} \subseteq \mathbb{R}^d$ , where  $\mathcal{Z}$  is the space of latent representation, and  $\text{Enc}$  and  $\text{Dec}$  are the encoder and decoder, respectively.

In our model,  $\text{Dec}$  is defined as a co-generation model of natural images and PAEs. Separate branches are created for the coding estimation of natural images and the coding generation for PAEs, denoted as  $\text{Enc}_N$  and  $\text{Enc}_P$ , respectively. For patch attack tasks, a lightweight MLP module on the vision backbone (e.g. ResNet) features is implemented as the encoding

modules. To fuse the feature extraction of  $\mathbf{m}$  and  $X_{global}$ , an additional channel for  $\mathbf{m}$  in the feature extractor of  $X_{global}$  is inserted. For  $P_X = [X_{local}; X'_{global}; \mathbf{m}']$  and  $\lambda$ ,  $\text{Enc}_P$  is formulated as:

$$\begin{aligned} \text{Enc}_P := & \text{MLP}_1(\text{LN}(\text{MLP}_2(\text{ResNet}_1(X_{local})))) \\ & + \text{LN}(\text{MLP}_3(\text{ResNet}_2(\text{Concat}[X_{global}, \mathbf{m}']))) \\ & + \text{MLP}_4(-\log(\max\{\lambda, \exp(-10)\}))), \end{aligned} \quad (22)$$

where  $\text{Resnet}_2$  is initialized with the pre-trained weights and  $\text{Resnet}_1$  is trained from scratch, and Layer-norm ( $\text{LN}$ ) is been applied to balance the inductive bias between global and local features.  $\text{Enc}_N$  is constructed by  $\text{MLP}_5 \circ \text{ResNet}_1$  and can assist the training of  $\text{Enc}_P$  with parameter sharing. We acknowledge that only a simple but representative neural network architecture is presented, which can be replaced by more complex designs to improve performance and speed. The  $\text{Enc}_P$  network can be further scaled up with Transformer models if the feature set is defined as a sequence of vectors.

We design the latent space  $\mathcal{Z}$  as a 512-dimensional vector. We employ *resnet18* and *resnet50* with checkpoint provided by *torchvision* as for *ResNet*<sub>1</sub> and *ResNet*<sub>2</sub>, respectively, and do not freeze their parameters during the training. For the decoder, we implemented a more lightweight model following the architecture of *BigGAN*. We use 3 up-sampling *ResBlocks* with extra contextual path inserted from the high-level representation  $z$  and then adapt 2 consecutive transposed convolutional layers to expand the output patch size to 256x256 from the 8x8 feature map, which is generated with the module *Linear - Unflatten - TransposeConvBlock* from the latent vector. For the patch attack scenario, we resize both the local and global input from the attacker's observed picture into 256 × 256 and the patch generated is also 256 × 256. For the CARLA simulation scenario, we simply set both the local and global content as the whole observation since the perturbed area (the entire car texture) is larger, and we use the same resolution as the patch scenario and resize the PAE to the original scenario during evaluation.

**Model Training of DynamicPAE:** We implement *DynamicPAE* with PyTorch Lightning, use Adam optimizer with the default parameters (lr=1e-3), set batchsize=32, and train for 256 epochs. All training and evaluation is done with one or two NVIDIA GPU(s) with Ampere architecture. The training is simple to implement since no gradient operation and additional discriminators have been introduced. Some of the key points are: ① *BatchNorm* module provided by *PyTorch* is adapted as a streaming algorithm to estimate statistics for skewness during training steps. ② Parameter freezing, including *BatchNorm*, is executed on the victim model for consistency, and *GradientNorm* is performed on the patch to prevent gradient vanishing. ③ Affinity transformation and reversed affinity transformation are performed with *torch.nn.functional.gird\_sample* for patch injection, mask encoding, and patch background extraction. ④ The training step is skipped if the *nan* or *inf* gradient occurs to stabilize the experiment of the infinite gradient.

---

**Algorithm 1:** DynamicPAE Training

---

**Input:** Dataset  $\mathcal{D} \subset \text{Images} \times \text{BBoxes}$ , Target model  $\mathcal{F}$ , Untrained PAE generator  $\mathcal{G}$

**Output:** Trained model  $\mathcal{G}$

```

1  $\alpha \leftarrow 1.0$ 
2 for epoch  $\in \{1, 2 \dots n\}$ , step  $\in \{1, 2 \dots m\}$  do
3   Sample  $X$  from the dataset  $\mathcal{D}$ .
4    $\mathcal{L}_{vae} \leftarrow \beta$ -VAE loss [56] with encoder  $\text{Enc}_N$ , decoder  $\text{Dec}$  and data  $X$ .
5   Sample task ratios  $\lambda$ .
6   Pre-process  $P_X$ .
7   Generate PAE  $\delta \leftarrow \text{Dec} \circ \text{Enc}_P(P_X)$ .
8   Compute loss matrix  $\mathbf{L}(X \oplus (\delta, \theta), \mathcal{F})$ .
9    $\mathcal{L}_{reg} \leftarrow \gamma \cdot \|\mathbf{Z}\|_2^2 + \mathcal{L}_{TV}$ .
10   $\mathcal{L}_{GCA} \leftarrow \sum_{i=1}^b \sum_{j=1}^t \{\lambda \alpha^T \otimes \mathbf{L}\}_{i,j}$ .
11   $\mathcal{L}_{total} \leftarrow \mathcal{L}_{GCA} + \mathcal{L}_{reg} + \mathcal{L}_{vae}$ .
12  Optimize  $\mathcal{G}$  with  $\nabla \mathcal{L}_{total}$  using Adam.
13  Optimize  $\alpha$  with  $\nabla \alpha := -\text{skewness}(\mathcal{L}) + \varsigma$  using Adam.
14 return  $\mathcal{G}$ .

```

---

**Baseline Attack Methods:** For the novel task of dynamic attack, we select representative methods as baselines and adapt them to the test setup including *PGD* [59], *AdvGAN* [37], *GAN-NAP* [42], also known as *NAP*, and *T-SEA* [43]. The comparison of these methods is shown in Table 15. *PGD*, *GAN-NAP*, and *T-SEA* are adapted as patch-form PAE evaluation baselines. For *CARLA* experiment, we conducted supplementary evaluations on similar *AdvGAN* methods. For the physical experiment, we performed tests using existing patch attacks (*GAN-NAP* and *T-SEA*).

**Baseline Method Implementations:** For *GAN-NAP*, we integrate it into our framework with its default hyperparameters and use our attack transformation pipeline and attack loss to enhance its performance.

For *T-sea*, we use its framework for training because it performs better due to the overall effect of its tuned augmentation pipeline, and we slightly modified its transformation parameters to match our evaluation. To further align the evaluation between *T-sea* and our model, we use the ShakeDrop modified detectors provided by *T-sea*, which aims

**Table 15: Comparison of different baselines.** PGD (with Expectation-over-Transformation (EoT) ) is considered to be adaptive and physically capable despite its speed.

Baselines	PGD	AdvGAN	T-SEA	GAN-NAP
DNN based	✗	✓	✗	✓
Physical Capability	✓	✗	✓	✓
Adaptive	✓	✓	✗	✗
Patch Attack	✓	✗	✓	✓
Perturbation	✓	✓	✗	✗

to enhance transferability and may sacrifice aggressiveness, into our framework to ensure consistency. Since Yolo-v8 is not integrated into *T-sea*, we transplanted it into the *T-sea*'s framework (without ShakeDrop). For *PGD*, we adapt the *UPGD* implementation in *torchattack* [86] and adapt the parameters  $step = 2048, \alpha = 10/2048$  to fit the random patch transformations in the main benchmark. For *AdvGAN*, we follow the original codes and related libraries for implementation. We directly used the original hyperparameters and, after tuning, verified that they remained approximately optimal in the new scenario.

**Victim Models:** To validate our method, we select a diverse set of object detection models: Faster R-CNN, YOLOv3-m, YOLOv5-m, YOLOv5-s, and YOLOv8-n. These models vary in size, version, and architecture. Table 16 compares these models. Parameters and FLOPs were calculated using the *thop* library, and mAP<sub>50</sub> was reported on the COCO dataset. Faster R-CNN, pre-trained on an earlier COCO version, is excluded from the assessment.

**Table 16: Comparison of object detectors.**

Model	Faster-RCNN	Yolov3-m	yolov5-m	yolov5-s	yolov8-n
Arch.	two-stage	one-stage	one-stage	one-stage	one-stage
Param. Size	41.76M	61.95M	21.19M	7.24M	3.16M
FLOPs	267.37G	105.40G	49.08G	16.54G	8.7G
mAP <sub>50</sub>	–	57.91%	64.13%	56.79%	53.25%

## 2 EXPERIMENT RESULTS

### 2.1 Physical Attack Visualization

We design an experiment to further show the real-world adaptation capability of our framework. The patch generator runs on a laptop equipped with NVIDIA 4050 GPU, and inference in real-time, and the victim model *YOLO-v5s* is run on another laptop. We varied the attack environment by controlling the room lighting while the experimenter tested the performance of the adversarial example through a handheld display. As shown in Figure 11, the dynamic adaptation feature of *DynamicPAE* is been realized and achieved higher attack performance in both lighting conditions. Furthermore, since indoor lighting changes cause significant changes in the exposure parameters of the camera deploying the target detection model, it creates further challenges for attack robustness. Although we did not perform detailed simulations of exposure changes, the adversarial example generated by our model is still able to maintain robustness.

To further evaluate the robustness in the physical world, we present an experiment on *DynamicPAE* that used a fixed value of  $P$  as a substitute and jittered the screen within a certain range. Our PAE still maintains its attack effectiveness under these conditions, demonstrating the robustness of our model. The demonstration is shown in Figure 12.

**Video Analysis:** We have included a total of 4 videos in the video supplementary material *Videos.zip* to support the experiment. In *physical\_exp.mp4* and *physical\_exp\_1.mp4*, we selected the physical adversarial patches generated by *GAN-NAP* and *TSEA* for comparison, and the training process is as same as the benchmark setting *Base+*. It is very apparent that in both dynamic background and moving person scenarios, the attack performance of static PAEs is limited. In contrast, our *DynamicPAE* ensures sufficient attack capability. In *physical\_exp\_2.mp4*, we did not provide the model with precise screen coordinates as input. Instead, we used a fixed value as a substitute and jittered the screen within a certain range. Our PAE still maintains its attack effectiveness under these conditions, demonstrating the robustness of our model. In *physical\_exp\_3.mp4*, we compare static PAE and the PAE generated by *DynamicPAE*. In response to changes in lighting, our *DynamicPAE* rapidly changes the presented PAE to maintain attack performance, and superior attack capabilities compared to static attacks are achieved.

### 2.2 Latent Interpretation

**Correlation Interpretation:** To interpret the learned correlation, we perform analysis based on the latent representation  $Z$ . The analysis of the learned correlation is performed on the COCO dataset with the setting of Yolov5s-Base and  $\lambda_{atk} = 1.0$ . To visualize the representation, we first annotate the latent representations based on the style of PAEs since no ground-truth label is available, and then we apply *LDA* for dimension reduction. The result is shown in Figure 13a, indicating that the model successfully learns a linearly decomposable representation of PAEs. We further conduct the K-nearest neighbor (KNN) search ( $k=3$ ) in the dimension-reduced space and visualize the corresponding physical context in Figure 13b. The

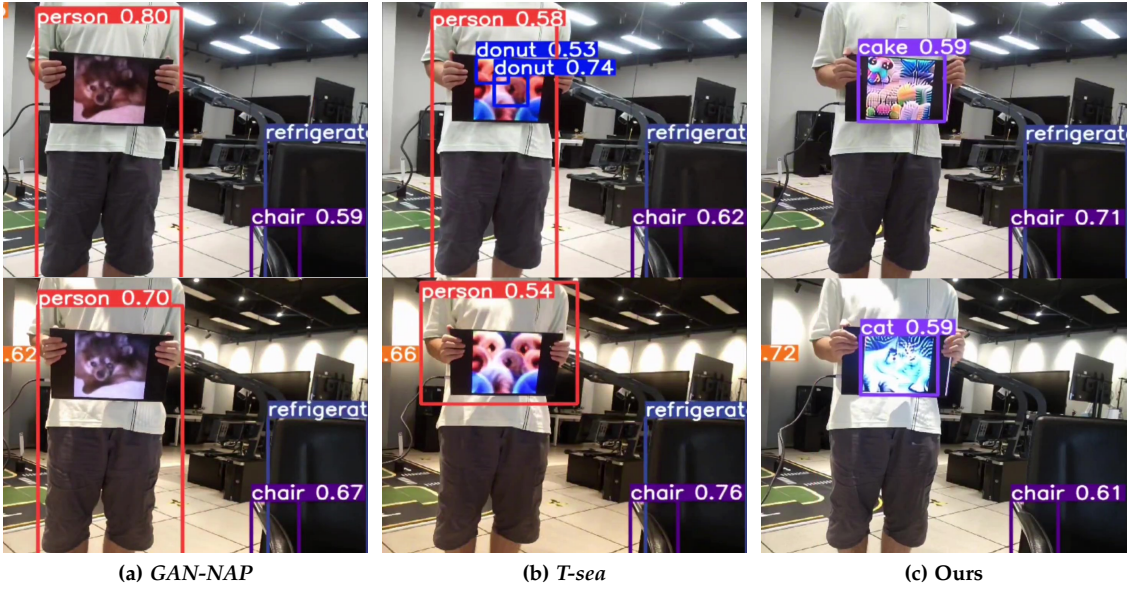


Figure 11: In the scenario of the different lighting (row 1 & row 2), our method achieves better attack performance and adapts the lighting dynamically.

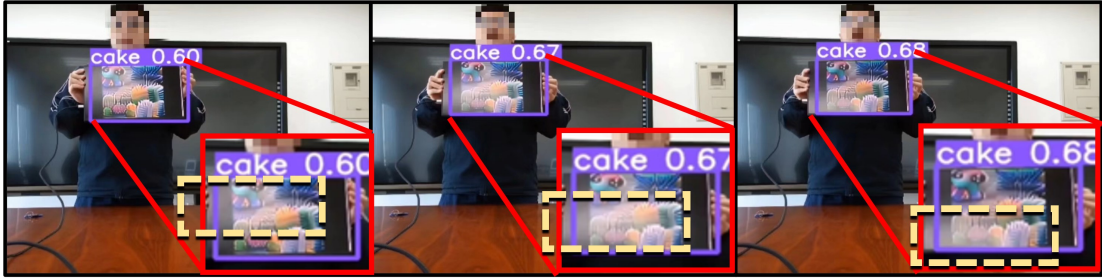


Figure 12: Illustration of physical robustness under different reflections (marked with yellow boxes).

outcomes demonstrate that the KNN result has significant similarity with the KNN query in terms of certain characteristics, including human actions, the chromatic attributes of clothing, and the exposed body parts *et al.*, and the generated PAE is also similar, indicating that our model successfully establishes a distinction between physical contexts  $P$  based on the vulnerability of the target model by learning PAE generation, and thus the fuzzy mapping between  $P$  and PAEs  $\delta$  is constructed.

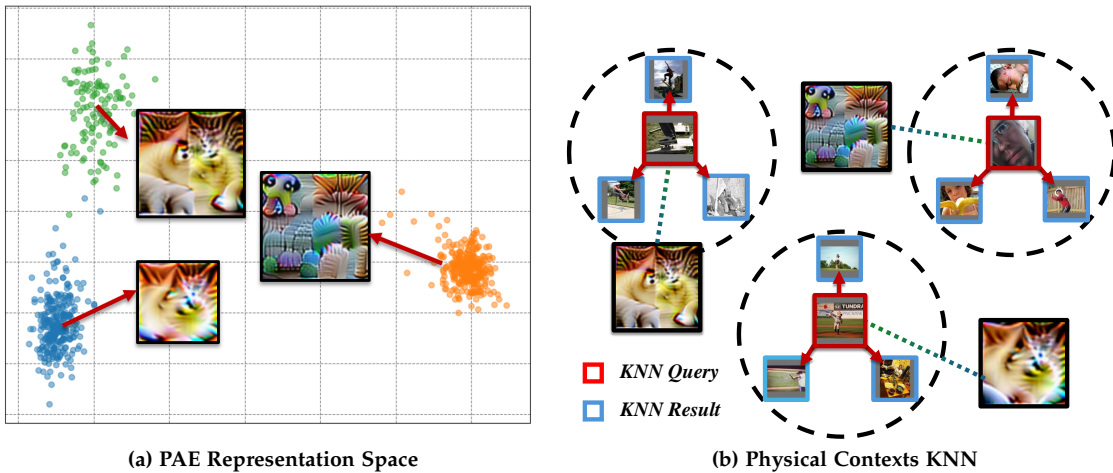
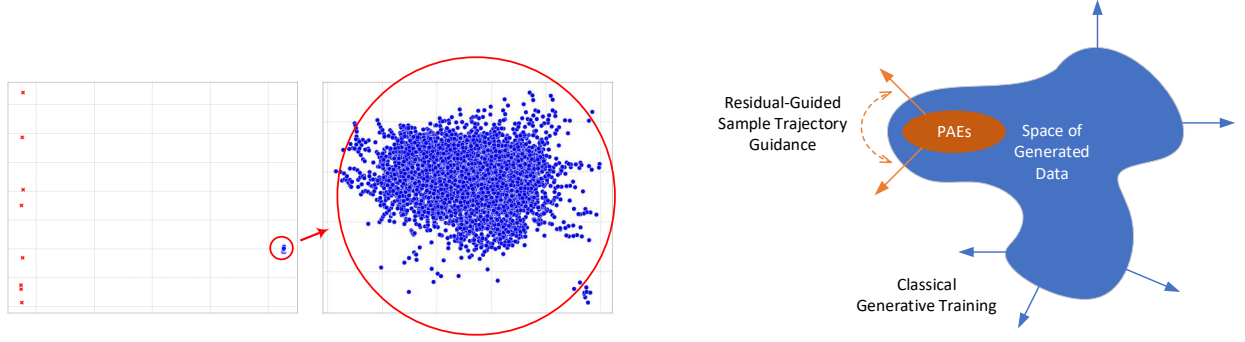


Figure 13: Visualization of learned correlation through latent representation.

**Latent Evasion Interpretation:** As discussed in section 4.3.2 of the main paper, the *latent evasion* problem is a new problem in training dynamic PAE generators. We visualize the latent representations with PCA. As shown in Figure 14a, the representation distribution tends to move away from the center, causing the phenomenon of infinite gradients. This phenomenon is related to the specificity of the training task, as our framework explores the novel PAE patterns that may not exist in the dataset (illustrated in Figure 14b). Moreover, the exploration is performed under noisy and imbalanced gradient feedback, leading to latent instability. Therefore, additional regularization is required for stabilized training.



(a) Visualization of latent evasion. The red crosses denote the case without soft regularizing  $z_{adv}$  and only clip it within  $(-2, 2)$ , leading to gradient explosion, while the blue dots denote the regularized representation.

(b) Illustration of the space of generated data. Our residual-task guided training method enables the exploration of dynamic PAEs, and these PAE patterns may not exist in the dataset.

Figure 14: Analysis for the Latent Evasion Problem

### 2.3 Experiments on More Benchmark Settings

We further evaluate different transformation parameters. The Attack-Distortion curves for two datasets are presented in Figure 15m and Figure 16. The experimental results further support the superiority of our model, except PGD performs better in zero spatial transformation since this setting is more like a digital attack.

## 3 CONVERGENCE OF HYPER-PARAMETER SCHEDULER

We aim to optimize the following multi-objective loss function, where  $\lambda$  is sampled by a certain distribution, and we aim to control the hyper-parameter  $\alpha$ . This section shows the convergence of the controller.

$$\mathcal{L} = \alpha\lambda\mathcal{L}_{\text{Inv}} + (1 - \alpha)(1 - \lambda)\mathcal{L}_{\text{Atk}} \quad (23)$$

We assume that  $\mathcal{L}_{\text{Inv}}, \mathcal{L}_{\text{Atk}} > 0$ . For any *optimal* PAE solution  $\delta(\lambda)$  with minimum  $\mathcal{L}$  under a certain hyper-parameter setting, we assume that when  $\mathcal{L}_{\text{Atk}}$  is higher, then  $\mathcal{L}_{\text{Inv}}$  is lower. Then, we define:  $\mathcal{L}_{\text{Atk}} = f(\mathcal{L}_{\text{Inv}})$ .

We formalize the *optimal* as follows. Note that it is slightly different from the *Pareto optimal*. For any pair of loss  $(\mathcal{L}_{\text{inv}}, \mathcal{L}_{\text{Atk}}) = (x, f(x)), (y, f(y)),$  or  $(z, f(z))$  s.t.  $0 < x < y < z$ , there must exist  $a = \alpha\lambda > 0$  and  $b = (1 - \alpha)(1 - \lambda) > 0$  s.t.  $y$  is smaller than both  $x$  and  $z$  in the value of  $\mathcal{L}$  parameterized by  $a$  and  $b$ . Otherwise, there will not be any parameter  $a > 0$  and  $b > 0$  that let  $(\mathcal{L}_{\text{inv}}, \mathcal{L}_{\text{Atk}}) = (y, f(y))$  corresponds to any of the optimal  $\delta(\lambda)$ . This leads to the concave property of  $f$ . Specifically, if  $y$  is more *optimal* than  $x$  under loss parameters  $a$  and  $b$ , we have:

$$ay + bf(y) < ax + bf(x) \Rightarrow -\frac{a}{b} > \frac{f(y) - f(x)}{y - x}, \quad (24)$$

and if  $y$  is more *optimal* than  $z$  under loss parameters  $a$  and  $b$ , we have:

$$ay + bf(y) < az + bf(z) \Rightarrow -\frac{a}{b} < \frac{f(z) - f(y)}{z - y}. \quad (25)$$

Thus,

$$\frac{f(z) - f(y)}{z - y} > \frac{f(y) - f(x)}{y - x}, \quad (26)$$

and consequently,  $f$  is concave, that is,  $f'' > 0$ . The expression of  $f'$  can be derived with:

$$\frac{\partial \mathcal{L}}{\partial \mathcal{L}_{\text{Inv}}} = \alpha\lambda + (1 - \alpha)(1 - \lambda)f'(\mathcal{L}_{\text{Inv}}) = 0, \quad (27)$$

and if  $\lambda, \alpha \notin \{0, 1\}$ ,

$$f'(\mathcal{L}_{\text{Inv}}) = -\frac{\alpha\lambda}{(1-\alpha)(1-\lambda)}. \quad (28)$$

Then we have:

$$\frac{\partial \mathcal{L}_{\text{Inv}}}{\partial \alpha} = \frac{\partial \mathcal{L}_{\text{Inv}}}{\partial f'(\mathcal{L}_{\text{Inv}})} \cdot \frac{\partial f'(\mathcal{L}_{\text{Inv}})}{\partial \alpha} = \frac{1}{f''(\mathcal{L}_{\text{Inv}})} \cdot -\frac{\lambda}{1-\lambda} \cdot \frac{1}{(1-\alpha)^2} < 0. \quad (29)$$

And  $\frac{\partial \mathcal{L}_{\text{Inv}}}{\partial \alpha} = 0$  when  $\lambda \in \{0, 1\}$ . Recall that the control function of  $\alpha$  is defined as:

$$\nabla \alpha := -\text{skewness}(\mathcal{L}) + \varsigma, \quad \text{skewness}(\mathcal{L}_{\text{inv}}) := \mathbb{E}\left[\frac{(\mathcal{L}_{\text{inv}} - \mu(\mathcal{L}_{\lambda=0,1}))^3}{\sigma(\mathcal{L}_{\lambda=0,1})^3}\right] \quad (30)$$

Thus,

$$\nabla^2 \alpha = -\frac{\partial \text{skewness}(\mathcal{L})}{\partial \alpha} = -\mathbb{E}\left[\frac{\partial(\mathcal{L}_{\text{inv}} - \mu(\mathcal{L}_{\lambda=0,1}))^3}{\partial \mathcal{L}_{\text{inv}} \cdot \sigma(\mathcal{L}_{\lambda=0,1})^3}\right] \cdot \frac{\partial \mathcal{L}_{\text{inv}}}{\partial \alpha} > 0. \quad (31)$$

And the optimization of  $\alpha$  is able to converge by limiting its range.

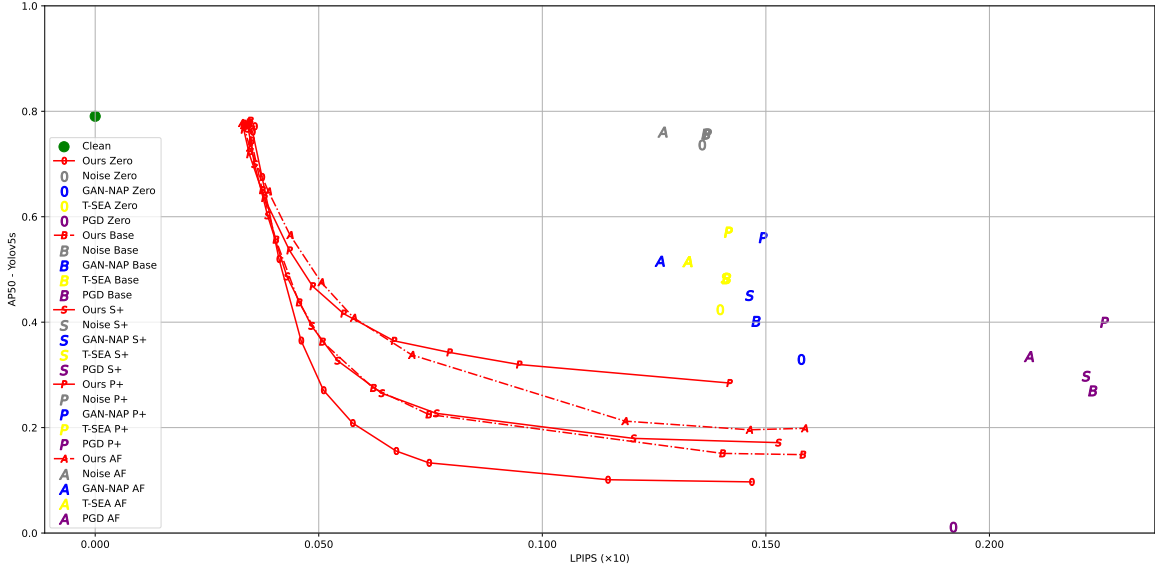


Figure 15: Evaluation results on COCO dataset with different transformations. The target model is Yolov5s.

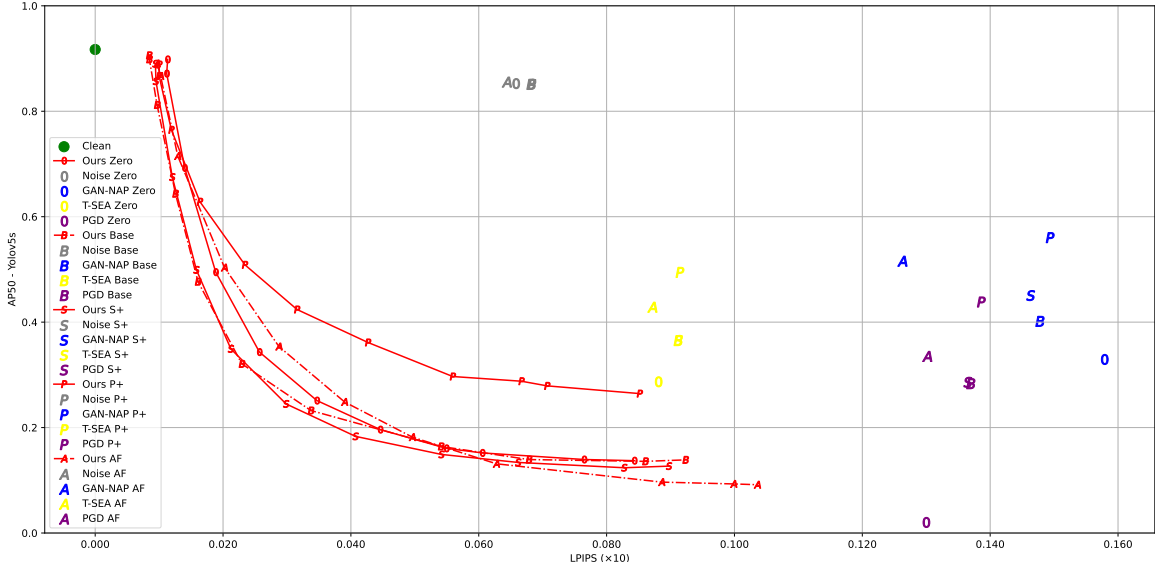


Figure 16: Evaluation results on Inria dataset with different transformations. The target model is Yolov5s.